Andreas Kottlan, BSc

DEM Contact Model Parameter Calibration based on Experimental Bulk Property Analysis

MASTER'S THESIS

to achieve the university degree of

Diplom-Ingenieur

Master's degree program: Chemical and Process Engineering

Submitted to

Graz University of Technology

Supervisor

Univ.-Prof. Dipl.-Ing. Dr. techn. Johannes Khinast
Institute of Process and Particle Engineering

Co-Supervisor

Dipl.-Ing Dipl.-Ing. Peter Loidolt

Institute of Process and Particle Engineering

Graz, June 2018

AFFIDAVIT

I declare that I have authored this thesis independently, that I have not used other than the declared sources/resources, and that I have explicitly indicated all material which has been quoted either literally or by content from the sources used. The text document uploaded to TUGRAZonline is identical to the present master's thesis.

Date	Signature

Abstract

The success of every industrial process depends on the ability to handle the materials involved. Trying to characterise these materials by the commonly known states of matter, i.e. gaseous, liquid and solid, one faces a challenge as it comes to powders. At the first glance, powders clearly are solids, but looking at the bulk behaviour, also liquid-like behaviour can be observed. Due to this and the fact that powders are involved in about 75% of all industrial processes, high effort is put in the understanding and correct prediction of powder behaviour. A state of the art technique in this field is DEM simulation. Even though this method is commonly used, the correct quantitative prediction of powder behaviour is still a challenge. The present work investigates the possibility to provide generally valid models for specific powders by running a calibration procedure using metrics yielded by small scale powder experiments. The major challenge observed is the modelling of the influence of particle shape on the shear resistance of the investigated lactose powders. In the used soft sphere approach, the shape was modelled using friction, rolling resistance and cohesion models, which led to unsatisfactory results. As this modelling does not seem to account for all physical processes within the powder a generally valid model could not be created using this approach. Therefore, the major finding of the present thesis is, that particle shape needs more physical modelling, i.e. the use of non-spherical particles in simulation.

Kurzfassung

Der Erfolg jedes industriellen Prozesses hängt von der Fähigkeit ab, mit den verwendeten Materialien umzugehen. Wenn man versucht, diese Materialien in die allgemein bekannten Aggregatzustände, gasförmig, flüssig und fest, einzuordnen, steht man vor einer Herausforderung, wenn es um Pulver geht. Pulver bestehen einerseits aus festen Partikeln, andererseits zeigen Pulverschüttungen ein flüssigkeitsähnliches Verhalten. Aufgrund dieser Eigenschaft und der Tatsache, dass Pulver in etwa 75% aller industriellen Prozesse eine Rolle spielen, wird ein hoher Aufwand für das Verständnis und die korrekte Vorhersage des Pulververhaltens betrieben. DEM Simulationen sind für diesen Anwendungsbereich Stand der Technik. Obwohl diese Methode häufig angewandt wird, ist die korrekte quantitative Vorhersage des Pulververhaltens immer noch eine Herausforderung. Die vorliegende Arbeit untersucht die Möglichkeit, allgemeingültige Modelle für einzelne Pulver zu liefern, indem eine Kalibration an Messergebnissen einfacher Laborversuche durchgeführt wird. Die wichtigste beobachtete Herausforderung ist die Modellierung des Einflusses der Partikelform auf die Scherfestigkeit der untersuchten Laktosepulver. Bei dem verwendeten Soft-Sphere-Modell wurde die Partikelform anhand von Reibungs-, Rollwiderstands- und Kohäsionsmodellen modelliert, was zu unbefriedigenden Ergebnissen führte. Da diese Modellierung nicht alle physikalischen Vorgänge im Pulver abzubilden scheint, konnte mit diesem Ansatz kein allgemein gültiges Modell erstellt werden. Das wichtigste Ergebnis der vorliegenden Arbeit ist daher, dass die Partikelform eine physikalischere Form der Modellierung erfordert, und zwar die Verwendung von nichtsphärischen Partikeln in der Simulation.

Acknowledgement

First of all, I want to thank Peter Loidolt who is responsible for my not too short intermezzo with DEM-simulation. He provided a topic which allowed me to gain insight in the strengths, weaknesses and possibilities of a commonly used method. If the weaknesses started to drain my believe in the feasibility of some problems Peter either provided ideas for a new approach or sometimes stopped me from chasing an idea.

I would like to thank Prof. Johannes Khinast for giving me the opportunity of writing my thesis at the IPPE, which is not only an excellent scientific facility but also a family-like microcosmos.

Within this microcosmos I spent most time with Andreas B., Daniela F., Peter and Stefan M., who shared the office with me and who I'd like to thank for countless funny and inspirational conversations. Andreas and Stefan supported me making my first steps in LIGGGHTS® which was a great help. On this topic thanks also go to Ass. Prof Stefan Radl who provided me with deep insights on LIGGGHTS® when other sources ran dry.

Special thanks go to my family for their support throughout my whole study and especially in the challenging last months.

Table of Contents

1 Introduction

The behaviour of granular systems affects processes in nearly every industry. No matter if we look at the food industry, handling powders like sugar or corn starch, at metallurgy, using metal powders for sintering processes, or at the pharmaceutical industry using mixtures of active pharmaceutical ingredients and excipients for drug manufacturing. This list could be carried on, filling a thesis by itself. Due to the crucial impact of powder behaviour, a lot of effort was put into its understanding over the last decades. This led to many different approaches trying to model and predict how a granular system will behave under certain conditions. Even though this thesis focuses on the Discrete Element Method (DEM) proposed by (Cundall & Strack 1979), also other approaches should be mentioned here.

Especially for applications with high relative densities and high loads and therefore high particle deformation, such as in sintering or tabletting processes, Multi Particle Finite Element Methods are common (Han et al. 2017; Gethin et al. 2001; Procopio & Zavaliangos 2005). MPFEM is capable of mechanistic deformation modelling and is therefore able to depict for example the rising tensile strength of compressed powder due to increasing contact area. In MPFEM each particle is modelled using a mesh of finite mesh cells. This leads to a high computational effort, even for low numbers of particles. To overcome this issue, the whole powder bed can be modelled using Finite Element Method (FEM) (Khoei & Lewis 1999; Li et al. 2001; Diarra et al. 2013). At this point the individual particles disappear and the powder bed is assumed a continuum. To use this method, it is necessary to define a constitutive model for the powder, accounting for the characteristic powder behaviour, e.g. hardening, effective friction between powder and surrounding parts and so on. To gain such constitutive models MPFEM can be used, as done by (Loidolt et al. 2018) FEM is less practical if it comes to large bed deformations, discontinuities within the bed and free surfaces. If these applications should be realised one has to apply additional tools to overcome systematic limitations of FEM, some of them addressed by (Oñate et al. 2008). The discussion of these tools is not within the scope of this thesis.

The DEM models a granular system discretised by the particles themselves. To describe the behaviour of the powder bed, the forces acting on each particle are calculated and afterwards applied on them to calculate velocity and displacement for the next time step. This leads to a high variability when it comes to the simulation setup, since the individual particles can move freely within the simulation box. There are no limitations in terms of a minimum relative density of the

system. Still, with DEM the computational effort is within reasonable bounds for up to a million particles. This makes DEM the state of the art for a wide field of applications, for example dosing (Loidolt et al. 2017), mixing (Radeke et al. 2010), granulation (Gantt & Gatzke 2005) or fluidised bed simulation using a coupling of DEM and computational fluid dynamics (CFD) (Girardi et al. 2016). An overview of further different DEM applications is provided by (Zhu et al. 2008).

In DEM based models the particles are not deformed, but the particles are allowed to overlap with each other. For the calculation of present forces contact models are needed, describing the interaction between two particles or a particle and a wall in contact. Within the last decades various contact models have been proposed, some reviews provided by (Di Renzo & Di Maio 2004), (Mishra 2003) and (Horabik & Molenda 2016). One of the most prominent ones to be mentioned is the model based on the work of (Hertz 1882), accounting for the non-linear behaviour of the contact force with increasing overlap, based on the analytical solution of elastic deformation of spheres. This model is also one of the standard contact models implemented in the used DEM simulation software LIGGGHTS® (Kloss et al. 2012).

Being an open source software LIGGGHTS® provides many possibilities to improve the modelling of powder behaviour. In the public release 3.8 besides other changes a new contact model is introduced, an implementation based on the model of (Luding 2008). The model will be discussed in the section *Methods and Materials.* Even though there are various differences between the available contact models, they all have in common the need for the specification of model parameters. These parameters account for example for particle stiffness, inter particle friction, particle size and shape and so on. Since neither particle size nor the exact shape is used in many simulations one cannot simply measure and use the real physical material properties. Due to this, for many applications it is necessary to calibrate the model parameters using experiments. (Coetzee 2017) provides a review of calibration methods used in scientific society. A very sophisticated method for calibration is presented by (Rackl & Hanley 2017). Despite this might be an efficient way to calibrate model parameters it is not used in this work, since a screening for the parameters with the strongest influence on the powder behaviour needed to be done first.

This screening is done using Design of Experiments (DoE) as introduced by (Fisher 1935). Because of the high number of parameters, the calibration is done using different experiments to lower the degree of freedom in optimisation on the one hand and to investigate different stress levels on the other hand. To keep the experimental effort at a reasonable level, commonly used

small scale experiments are used for calibration. Since the calibration of the simulated powder behaviour is only of value, if the determined parameters can be used for the simulation of a process of interest, a hopper discharge is modelled with the determined set of parameters, as it is also done for example by (Coetzee & Els 2009). The comparison of this simulation's result and the expectation of a widely used design approach is used as indication if the calibration is transferable.

The present thesis starts with the *"Methods and Material"* section (chapter 2) introducing the concept of DEM in detail in (2.1) prior to the introduction of the used contact models (2.2 and subsections). After this, the approach for particle scaling is presented (2.3) and an introduction to Calibration (2.4) and the Design of Experiments is given (2.5). Having explained the theoretical methods, the powders which shall be modelled are discussed (2.6). The last part of the *"Methods and Material*" section is the definition of the experimental and simulative setups which were used (2.7 and subsections) in the present work.

The results of executed experiments and simulations respectively are presented in the "*Results"* section (chapter 3), where at first a general comparison of different ways to create suitable initial powder beds is presented (3.1) before the "*Screening for important Parameters"* is discussed (3.2). This screening details on the influence of different model parameters on the outcome of different test setups. This subsection is followed by "*Calibration of the Powder Model"* detailing on the calibration process and the results for the calibrated models (3.3 and subsections). In the end of this section the results for a "*Hopper Discharge Simulation"* are presented to gain insight in the applicability of a powder model, calibrated in the presented way (3.4).

The conclusions which can be drawn from the findings and an outlook for future work are presented in the section *"Conclusions and Outlook"* (4)

2 Methods and Material

2.1 DEM

The discrete element method (originally distinct element method) or in short DEM is a numerical method making use of an explicit solving algorithm to describe the mechanical behaviour of granular media. As the name suggests, every particle is considered a discrete element with corresponding physical properties. The forces acting on each particle are determined by the contact forces between interacting particles and external force fields, e.g. gravity. To be able to apply an explicit solver, the used time step has to be chosen small enough to ensure that the calculated forces can be assumed constant for that time, and that the disturbance due to the contact does only affect the two interacting particles. In the present work the Rayleigh-time as defined in Eq. (1) was used to account for this with r being the particle radius, ρ the solid density, G the shear modulus and ν the Poisson ratio used for simulation.

$$t_{Rayleigh} = r\,\pi\,\sqrt{\frac{\rho}{G}}\,\frac{1}{0.163\,\nu\,+\,0.8766} \tag{1}$$

The interaction forces are calculated using a force-displacement relationship at the contact point, i.e. the contact model, afterwards Newton's second law is applied on the particles to calculate their movement. Here the naming interaction is used instead of contact, since the particles do not need to be in contact, to interact with another. As done in this thesis, also non-contact interactions like Van der Waals forces can be taken into account. To run these calculations, numerical simulation software packages are used. In the present thesis the open source software LIGGGHTS® was chosen. DEM uses a soft sphere approach, which means that particles might not deform, but they are allowed to overlap as depicted in Figure 1a). This overlap is then used to calculate the interaction forces, which can be divided into normal and tangential forces and torques due to rolling friction (Figure 1 b).

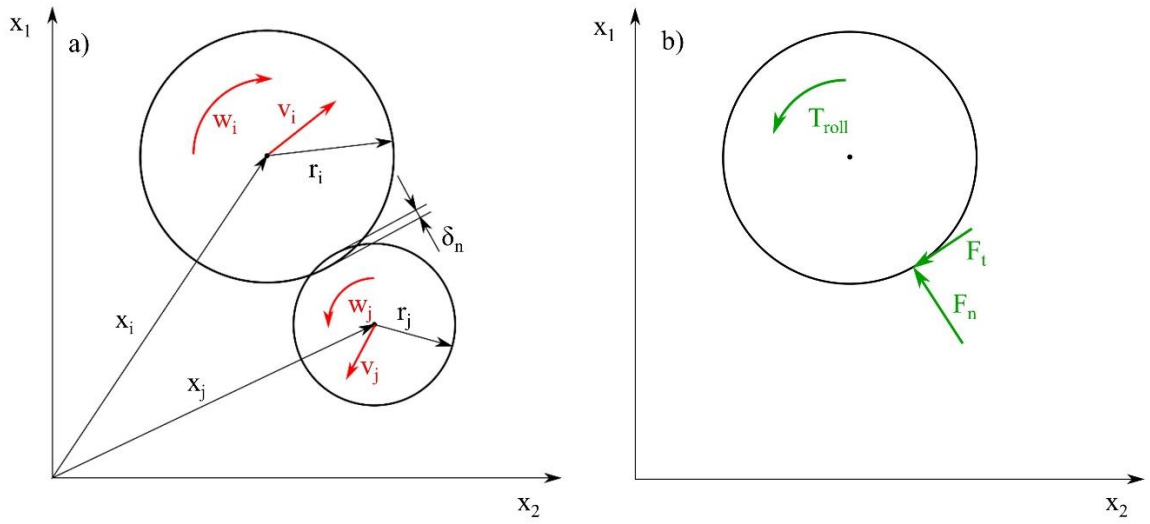

Figure 1: a) Two particles in contact with the positions x_i and x_j traveling with speeds v_i and v_j and the rotational speeds w_i and w_j, having an overlap of δ_n; b) Particle i with its reaction forces and torque

The way the interaction forces are calculated depends on the used contact model. The most common model is that of a spring-dashpot-model depicted in Figure 2.

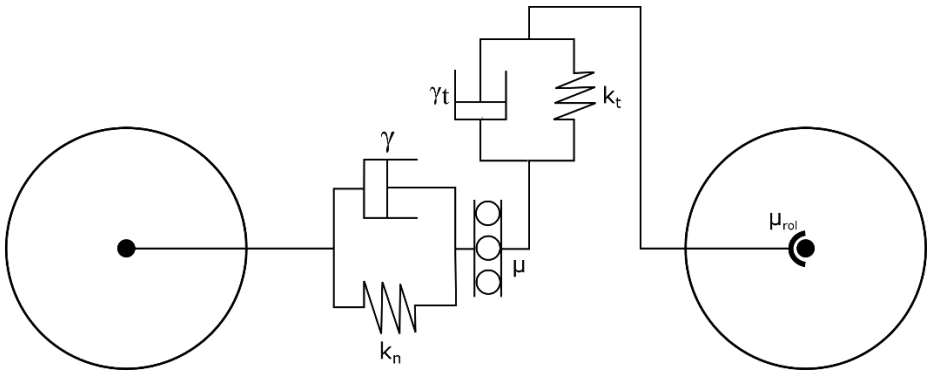

Figure 2: Scheme of a spring-dashpot model linking two spheres extended by a Coulomb criterion coupling and a joint modelling rolling friction

Here the model is extended by a coupling limiting the tangential force according to Coulomb's law for static and dynamic friction. Additionally, a constant directional torque is introduced acting against the direction of rolling, to model rolling friction. The contact model is explained 2.2 and subsections.

2.2 Contact Models

2.2.1 Luding Normal Model

In contrary to other contact models implemented in LIGGGHTS® the Luding normal model does not only account for repulsive forces in case of contact but also for attracting forces. The model

can be characterised as a piecewise linear hysteretic model (Luding 2008). For initial loading a constant normal contact stiffness k_1 and the normal overlap δ_n are used for force calculation – δ_n as defined by Figure 1 a and Eq. (2). Even though according to the Luding model the stiffness k_1 is no physical parameter, in this thesis it was calculated using the Young's modulus Y, a dimensionless overlap δ', defined as the ratio of overlap to particle radius, and the particle radius r in combination with the Hertz law for contact stiffness Eq.(3). This stiffness determines the contact force until one of the following two cases takes places. Case one, the overlap exceeds a maximum overlap δ^*_{max} defined by a dimensionless plasticity depth ϕ_f, the maximum stiffness k_2, the loading stiffness and the radii of the interacting particles r_i and r_j according to Eq. (4), resulting in a change to the maximum stiffness k_2. Case two, the overlap decreases, leading to a switch to the unloading branch of the hysteresis model. The unloading stiffness k_2 is determined using linear interpolation following Eq.(5). The unloading branch is truncated by the cohesion branch of the model closing the hysteresis cycle. The cohesion branch is defined by the cohesion stiffness k_c, modelling attractive forces if particles are in contact. Following this line, the force ends at the starting point, if the overlap reaches zero again. This starting point may be at zero force if no initial cohesion, also called pull of force f_0, is set. If a reloading occurs before the overlap has arrived at zero, the interpolated stiffness k^*_2 is used until $k_1 * \delta_n$ is met again. A corresponding overlap-force diagram is provided in Figure 3, the red line showing a high-load cycle and the blue one a low-load cycle. The grey line symbolises the boarders set for the contact force for given model parameters k_1, k_2, ϕ_f and k_c. Since no pull off force is considered using the Luding model the hysteretic force F_{hys} can be generally defined as in Eq.(6). Nevertheless, a pull off force is shown in Figure 3 to depict how δ_0 is determined if a pull off force is defined.

$$\delta_n = r_i + r_j - |\vec{x_i} - \vec{x_j}| \tag{2}$$

$$k_1 = \frac{4}{3} Y \sqrt{r^2 * \delta'} \tag{3}$$

$$\delta^*_{max} = \frac{k_2}{k_2 - k_1} \phi_f \frac{2 r_i r_j}{r_i + r_j} \tag{4}$$

$$k_2^* := k_2^*(\delta_{max}) = \begin{cases} k_2 & if\ \delta_{max} \geq \delta_{max}^* \\ k_1 + (k_2 - k_1)\dfrac{\delta_{max}^*}{\delta_{max}} & if\ \delta_{max} < \delta_{max}^* \end{cases} \quad (5)$$

$$F_{hys} = \begin{cases} k_1\,\delta_n & if\ \ k_2\,(\delta_n - \delta_0) \geq k_1\,\delta_n\ \&\ \delta_{max} < \delta_{max}^* \\ k_2^*\,(\delta_n - \delta_0) & if\ k_1\,\delta_n > k_2^*\,(\delta_n - \delta_0) > -k_c\,\delta_n \mid \delta_{max} > \delta_{max}^* \\ -k_c\,\delta_n & if\ -k_c\,\delta_n \geq k_2^*\,(\delta_n - \delta_0) \end{cases} \quad (6)$$

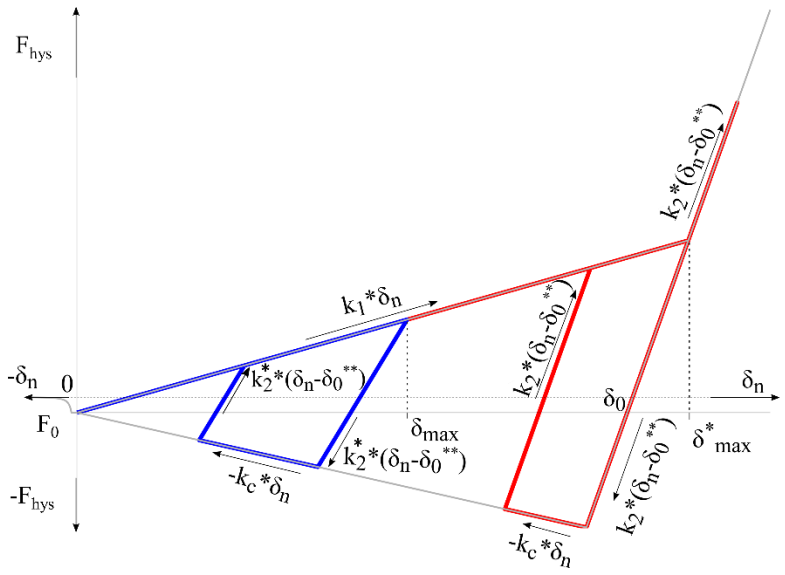

*Figure 3: Force-displacement diagram for the Luding normal model showing the bordering branches (grey), a high load (red) and a low load cycle (blue). ** δ_0 is defined for each straight-line intersecting with the imaginary horizontal line at f_0.*

As suggested by the spring-dashpot-model, also the Luding model considers a viscous contribution to the normal force. The damping force is modelled using a constant damping factor γ_n, calculated according to Eq. (7) - m_{eff} being the effective particle mass calculated as in Eq. (8) and e the coefficient of restitution - and the particles' normal relative velocity v_n. The calculated force always acts against the direction of relative motion. The resulting normal force due to the Luding contact model $F_{n,\,Luding}$ can be written as in Eq. (9). To be consistent with the implementation in LIGGGHTS® the maximum unloading stiffness k_2 and the cohesion stiffness k_c are not defined explicitly but by a factor and k_1 Eq. (10) and (11).

$$\gamma_n = \sqrt{\frac{4\, m_{eff}\, k_1}{1 + \left(\frac{\pi}{ln(e)}\right)^2}} \tag{7}$$

$$m_{eff} = \frac{2 m_i m_j}{m_i + m_j} \tag{8}$$

$$F_{n,Luding} = F_{hys} - \gamma_n \, \mathrm{v_n} \tag{9}$$

$$f_1 = k_2 / k_1 \tag{10}$$

$$f_2 = k_c / k_1 \tag{11}$$

2.2.2 Van der Waals Cohesion Model

Since the initial packing density of a powder bed can have a strong impact on different processes it is important to be able to produce initial packings with realistic relative densities. This is challenging for cohesive powders, as the particles need to be in contact with each other to exhibit cohesive forces in publicly available dry-powder-cohesion-models in LIGGGHTS®. This challenge also affected the work of (Bramböck 2017; Madlmeir 2018). (Parteli et al. 2014) did a study on the influence of Van der Waals forces on the relative density of particle packings dependent on the particle diameter. Due to the promising results of his study a corresponding interaction model was implemented in this work. The attracting force is calculated as given by Eq. (12), A_H being the Hamaker constant r_{eff} the effective radius according to Eq. (13) and D defined in Eq. (14) the surfaces distance of two particles. If D exceeds the cut off distance D_{max} the interaction is no longer considered to be active. Due to the formulation of F_{VDW} a minimal distance D_{min} needs to be defined, to prevent the force from getting infinite. Since the framework of LIGGGHTS® does not allow for non-contact interactions between particles and walls, only the non-contact interaction amongst particles was considered. This is assumed sufficient, since the influence of the wall on the bulk density is assumed to be negligible for the considered systems. Nevertheless, the maximum Van der Waals force determined by D_{min}^2 is used for approximation of a pull off force in sense of the Luding model. The introduction of this cohesion model leads the final formulation of the normal contact force as in Eq. (15). In the Results section the Van der Waals approach will be compared to three alternative methods of creating an initial packing. These approaches will be introduced together with the general setup for creating the initial packing.

$$F_{VDW} = \begin{cases} 0 & if\ D\ > D_{max} \\ \dfrac{A_H\, r_{eff}}{6\, D^2} & if\ D_{min} < D < D_{max} \\ \dfrac{A_H\, r_{eff}}{6\, D_{min}^2} & if\ D < D_{min} \end{cases} \quad (12)$$

$$r_{eff} = \frac{2 r_i r_j}{r_i + r_j} \quad (13)$$

$$D = -\delta_{\mathrm{n}} \quad (14)$$

$$F_n = F_{hys} - \gamma_n \, \mathrm{v_n} - F_{VdW} \quad (15)$$

2.2.3 Luding Tangential Model

This tangential model pursues the concept of a history-based overlap. This means, that the tangential relative displacement of two particles is integrated over one timestep and added to the tangential overlap of the last timestep see (16) . As depicted in Figure 2 the tangential force is modelled using a spring dashpot model with a tangential stiffness k_t and the tangential damping constant γ_t. For calculating the tangential force, the history-based overlap δ_t, and the relative tangential velocity v_t are then used. Furthermore, the tangential overlap is truncated to fulfil a yield criterion defined by Coulombs law of static and dynamic friction (17). The normal force used for the determination of this frictional force is not equal to the force calculated in (15) but is calculated using (18). Otherwise the force would equal zero for equilibrium if there is no external force acting on the particles. The implementation of this yield criterion is not fully consistent with the theoretical model according to a verification of (Madlmeir 2018). Despite this fact, the tangential model was used as implemented, since the effects on the bulk behaviour seem negligible and a reimplementation was not within the scope of this thesis. As for the normal model the tangential stiffness k_t, the coefficient of dynamic friction μ_d and the tangential damping coefficient γ_t are also defined by ratios

$$\delta_{t,new} = \delta_{t,old} + v_t * \Delta t \quad (16)$$

$$|k_t\, \delta_t| \leq F_{n,CC}\, \mu \quad (17)$$

$$F_{n,CC} = F_n + k_c * \delta_n + F_{VdW} \quad (18)$$

$$F_t = k_t\, \delta_t - v_t\, \gamma_t \quad (19)$$

$$f_3 = k_t/k_1 \quad (20)$$

$$f_4 = \mu_d/\mu_s \quad (21)$$

$$f_5 = \gamma_t/\gamma_n \quad (22)$$

2.2.4 Rolling Friction Model

For the reason of consistency, the Luding model for rolling friction was used in a first approach. Unfortunately, this model suffered from stability problems if the determining parameters were set to a level high enough to have an impact on the bulk properties of the simulated bed. To keep the number of input parameters at a manageable level the CDT model implemented in LIGGGHTS® was used, despite the drawbacks mentioned by (Ai et al. 2011). CDT means constant directional torque and as this suggests it models rolling friction by a torque independent on the tangential overlap or the relative velocity. The only dependency on the relative velocity is its direction which is set against the direction of rotational motion. This model needs only one input parameter, a coefficient of rolling friction μ_{roll}. The rolling torque is calculated following *(23)*, with $w_{r,shear}$ defined as the circumferential relative speed of the particles in contact, projected into the shear plane.

$$T_{roll} = -\mu_{roll}\, k_n\, \delta_n\, r_{eff}\, \frac{w_{r,shear}}{|w_{r,shear}|} \quad (23)$$

2.3 Particle Scaling

To reduce the computational effort and therefore make large scale applications feasible, the approach of coarse graining is commonly used in DEM applications. Using this approach, not every particle of the real powder is considered. The system is modelled by larger particles to reduce the number of particles. In this thesis the coarse graining is done by scaling the geometric setup as the radius of the spheres used in simulation was fixed to be 0.1 m. The relation of system dimension to particle radius was chosen such that an increase of the system size has only negligible influence on the simulation results.

As the particles, the investigated powders consist of, are in a diameter range of 5 – 200 µm a scaling approach was applied to the simulated spheres. This was done using a scale factor *SF* defined as in (24). With r being the radius used in simulation and r_{real} the radius of the real particles to be modelled. Having defined this scale factor, the scaling was done as described by Eq. (25)-(30). yielding the same forces for the particles with radius r as for the real particles.

$$r = r_{real}\, SF \tag{24}$$

$$\rho = \frac{\rho_{real}}{SF^3} \tag{25}$$

$$Y = \frac{Y_{real}}{SF^2} \tag{26}$$

$$A_H = A_{H,real}\, SF \tag{27}$$

$$D_{min} = D_{min,real}\, SF \tag{28}$$

$$D_{max} = D_{max,real}\, SF \tag{29}$$

$$\sigma = \frac{\sigma_{real}}{SF^2} \tag{30}$$

2.4 Calibration

To be able to model a real powder with the models mentioned above, a calibration of the used model parameters is performed. To do so, metrics considered useful to obtain fitting model parameters, are determined experimentally. A list of these metrics, the correlating experiments and the suspected influencing parameters are provided in Table 1. The definition of the metrics is provided in the correlating experiment descriptions.

Table 1: List of metrics used for calibration, corresponding experiments and suspected influencing parameters

Metric	**Experiment**	**Suspected influencing Parameters**
Compressibility	Compressibility Test	r_{real}, $A_{H,real}$, μ_{stat}, μ_{roll}, f_2
Confined Load Slope	Confined Compression Test	Y_{real}, f_1, ϕ_f
Confined Unload slope	Confined Compression Test	Y_{real}, f_1, ϕ_f
Tensile Strength	Tensile Test	r_{real}, $A_{H,real}$, f_1, f_2
Pre-Shear Stress	Shear Test	r_{real}, $A_{H,real}$, f_2, μ_{stat}, μ_{roll},
Slope of Yield Locus	Shear Test	r_{real}, $A_{H,real}$, f_2, μ_{stat}, μ_{roll},
Intercept of Yield Locus	Shear Test	r_{real}, $A_{H,real}$, f_2, μ_{stat}, μ_{roll},
Wall friction Angle	Wall Friction Test	$\mu_{stat,wall}$

2.5 Design of Experiments

Summing up the influencing parameters of the system we arrive at a number of 17, i.e. the Youngs's modulus Y_{real}, the Poisson's ratio ν, the density ρ_{real}, the radius r_{real}, the coefficient of restitution e, the plasticity depth ϕ_f the coefficient of static friction for particle-particle μ_s and for

particle-wall contact $\mu_{s,w}$, the coefficient of rolling friction μ_{roll}, the factors f_1 - f_5, the Hamaker constant $A_{H,real}$, Van der Waals cut off distance D_{max} and the Van der Waals minimum distance D_{min}. Five of these 17 parameters were chosen to remain constant, i.e. the density, the Poisson's ration, the coefficient of friction for particle-wall contact, D_{min} and D_{max}. This leaves us with twelve parameters to be varied. As described by (Bramböck 2017) the wall friction angle is mainly dependent on the particle-wall friction coefficient, and therefore the calibration of the wall friction angle is not done within the DoE framework, but after the determination of the powder model parameters.

2.5.1 Screening

To gain a meaningful insight into the change of the system behaviour when varying that many parameters a methodical approach is needed. In this thesis the decision fell on a fractional factorial DoE as described in (Kleppmann 2013). Explicitly a 2^{12-7} design was used. The use of this design allows to decrease the number of simulations to be run from 4097 for a full factorial design to 33 for the fractional (including a run with all parameters set to the mean values). This design is used to do a screening for the most relevant parameters. The strong reduction in effort is of course paid with a loss of information. A full factorial design yields all effects and interactions of the varied parameters separately. If a fractional design is used, the effects are confounded with each other. For the screening, the design was chosen such that effects of single parameters are only confounded with interactions of third order and higher, but second order interactions are confounded with other second and higher order interactions. Depending on how the effects and interactions are confounded with each other, the resolution of a fractional factorial design is defined in Latin numbers. For the present design the resolution is stated with IV. The full design is given in Table 17 in the Appendix.

2.5.2 Calibration

In a second step the number of varied parameters is reduced to eight, leaving Youngs's modulus Y_{real}, the radius r_{real}, the plasticity depth ϕ_f,the coefficient of static friction for particle-particle μ_s, the coefficient of rolling friction μ_{roll}, the factors f_1 and f_2 and the Hamaker constant $A_{H,real.}$ As the number of simulations is kept at 33 the resolution of the used 2^{8-3} design still is IV, but many important two parameter interactions are now only confounded with higher order interactions and can therefore be determined. The confoundation structure is provided by (NIST/SEMATECH 2012). The weighting of confounded two-factor interactions was done empirically.

The aim of this design of experiments is to gain equations of the form

$$y = y_{mean} + \sum_i b_i \, \Delta\xi_i + 2 \sum_k b_k \, \Delta\xi_{i,k} \, \Delta\xi_{j,k}$$

with

$$\Delta\xi_i = \xi_i - \xi_{i,mean}$$

relating the model input parameters *x* to each response *y* of the system. In this equation y_{mean} is the arithmetic mean of all responses for this simulation setup. While b_i characterises the impact of the single factors b_k characterises the impact of two factor interactions. For the given system of 8 factors, there are 8 constants b_i and 28 interaction constants b_k.

The determination of these constants is done by performing a regression analysis of the DoE results. To do so the impact of the single factors E_i and two parameter interactions E_k is evaluated by

$$E_i = \frac{\sum_h y_h - \sum_l y_l}{16}$$

$$E_k = \frac{\sum_{h,h} y_{h,h} - \sum_{l,h} y_{l,h}}{8} - \frac{\sum_{h,l} y_{h,l} - \sum_{l,l} y_{l,l}}{8}$$

For E_i the index *h* means the responses where factor *i* is at the high level and *l* means the low level. For the calculation of the interaction the difference between the effect of factor *i* for high factor *j* and the effect of *i* for a low *j* is calculated. Here the first index indicates the level of *i* and the second one the level of *j*. The constants are then calculated as

$$b_i = \frac{E_i}{\xi_{i,high} - \xi_{i,low}}$$

$$b_k = \frac{E_k}{(\xi_{i,k,high} - \xi_{i,k,low}) \, (\xi_{j,k,high} - \xi_{j,k,low})}$$

With these equations an optimisation of input parameters shall be done to find a parameter set which leads to the lowest deviation between the model and the real powder.

2.6 Powders to be modelled

Since it is the aim of the present work to investigate if free-flowing and cohesive powders can be modelled using a similar approach, powders relevant for industrial application were chosen to be modelled.

- Lactohale® 100 (LH100): A free-flowing lactose powder used as excipient for dry powder inhalation (DPI)
- Lactohale® 220 (LH220): A highly cohesive milled lactose powder used as excipient for dry powder inhalation (DPI)

The properties of LH100 and LH220 are stated in Table 2. These values are taken from (Das et al. 2013; DFE Pharma n.d.; DFE Pharma n.d.)

Table 2: Properties of the used lactose powders

	d_{10} [µm]	d_{50} [µm]	d_{90} [µm]	solid density [kg/m$^{3]}$
LH100	45-65	125-145	200-250	1545
LH220	1.5-3	11-15	25-40	1545

2.7 Simulations and Experimental Setup

Except for the creation of the initial packing, the simulation setups were designed to reflect their experimental equivalent. Therefore, the numerical and the experimental setups are presented together.

2.7.1 Initial Packing

The packing created in this step is the basis for all following simulations. A discrete particle size distribution as depicted in Figure 4 is assumed for the powder. The distribution is shifted to small particle diameters to better represent the fines contained in the powder.

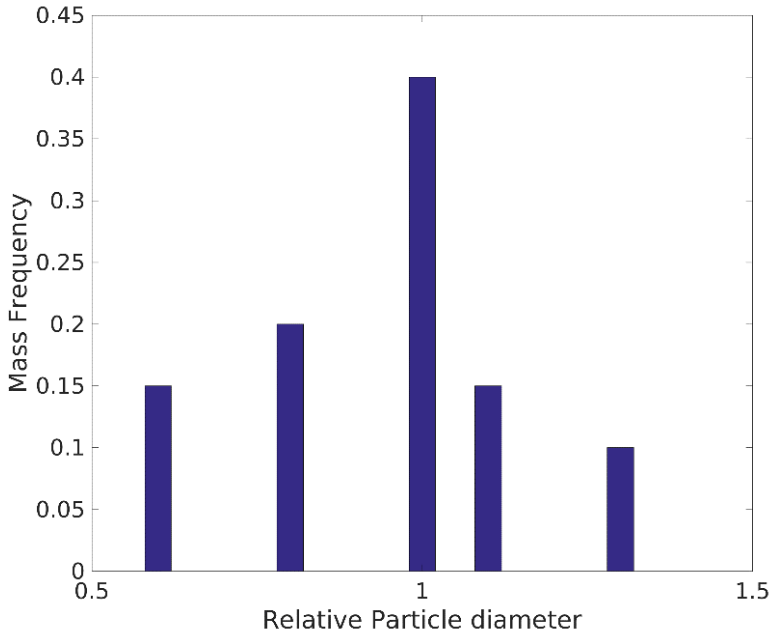

Figure 4: Discrete particle size distribution; mass based

The particles are randomly placed within the simulation box without overlap. The region for particle insertion was chosen cylindrical, since all experiments base on a cylindrical geometry. As the simulation is run in parallel processing mode, the box is separated in 16 subdomains. When placing the particles, the borders between these subdomains are kept empty. To homogenise the particle concentration within the simulation box the particles have a Gaussian distributed initial velocity. In a first step the particles are allowed to move freely, without cohesion or gravitational forces, until the subdomain borders vanish. After this step the particle motion is stopped, and the Van der Waals cohesion model is activated. There is still no gravitation. This allows the particles to form clusters and networks, which support the powder bed in the third step, i.e. settling. After the powder bed is static, the bed is cut off by changing the size of the simulation box. This reduced powder bed is then saved as restart file for the following simulations. The evolution of an exemplary powder bed can be seen in Figure 5. The particles are coloured according to the number of contacts with other particles, to indicate the increase of contacts due to formation of clusters induced by cohesive forces.

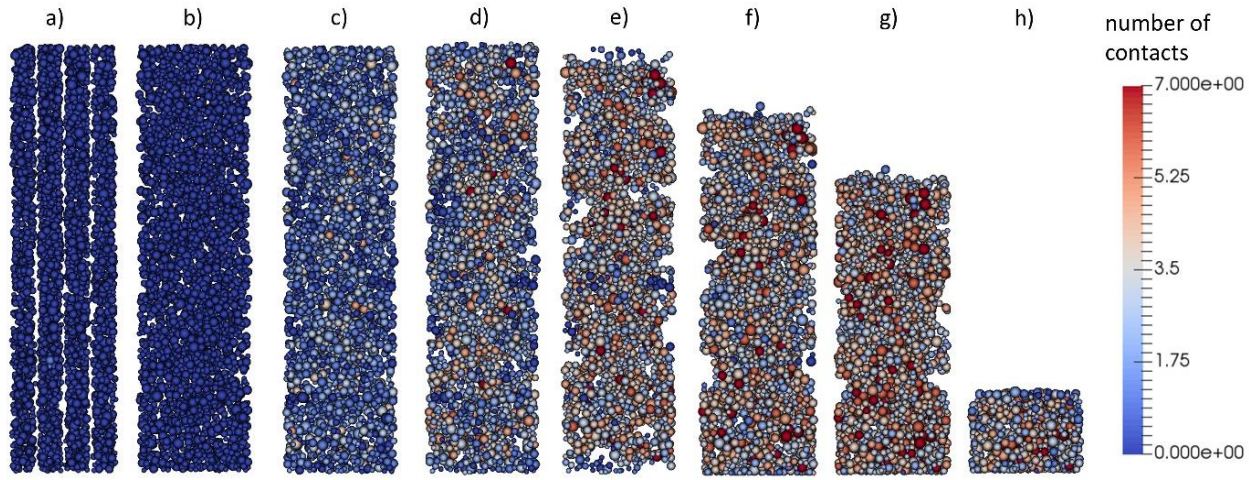

Figure 5: Evolution of a hexagonal assembly of cohesive particles in the described process for the creation of an initial packing

As mentioned in *"Van der Waals Cohesion Model"* different approaches to create an initial packing were tested.

1. Cluster formation due to Van der Waals forces
2. Promoting particle contact by random motion, only using a cohesive force when particles are in contact
3. Limiting the settling velocity in the concept of a terminal settling velocity for a specific particle size; cohesion when in contact
4. No contact promotion; cohesion when in contact – as benchmark

For the comparison of these approaches the simulation setup was adapted, to allow a faster simulation. The system size was decreased, a hexagonal box was used, and the boundary conditions were set periodic to balance the smaller system size. The simulation was adapted to the different approaches. Step 2 was not run for approaches 3 and 4. For the approach that uses the Gaussian distributed motion to create contact (approach 2), the motion was not stopped after step 1, but the cohesion (only interaction when in contact) was activated. For the limited settling velocity approach (approach 3), the run time for settling was increased to ensure that the particles are completely settled.

2.7.2 Confined Compression Test

The confined compression test provides more information about a powder, than a simple compressibility test. The compressibility is a metric depending on two other ones, i.e. the initial packing density and the highest solid fraction that can be reached by simple compression. Besides

the compressibility, the confined compression test can give information on the confined bulk stiffness, which is suspected to be useful for the calibration of the Youngs modulus and the unloading stiffness k_2. Furthermore, the shape of the stress/strain curve could provide additional information on the non-linear stress/strain relation of the powder. The confined compression test is also commonly used in literature, for example by (Coetzee 2016) and (Coetzee & Els 2009).

The real experiment is conducted using a rotary rheometer of the Anton Paar *MCRXX2*-series in combination with an Anton Paar *"Powder Cell"*. This setup is presented in Figure 6a. For compression a piston with exchangeable compression plate is used. A permeable plate made of sintered stainless steel (Figure 6b) is used for the compression test, allowing the air within the powder bed to escape while compression. The travelled distance as well as the normal force is recorded and evaluated to result in a stress-strain diagram.

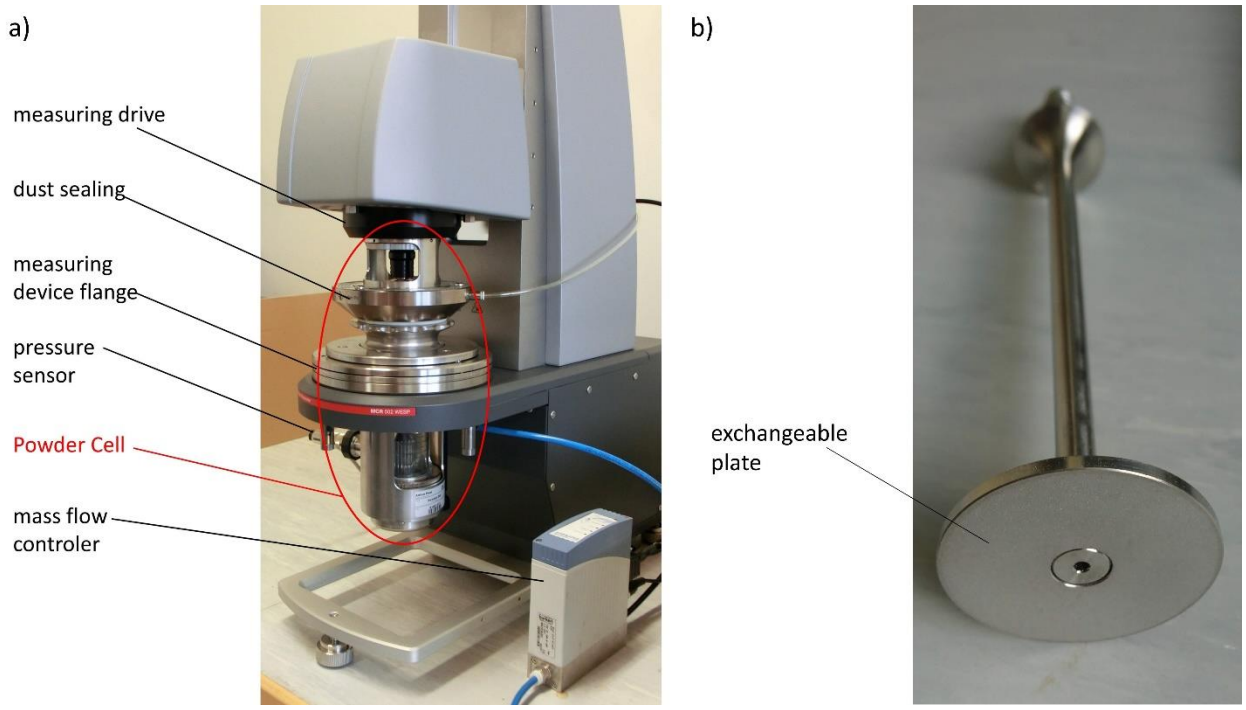

Figure 6: Measuring setup used for confined compression and the tensile tests; a) Photograph showing an Anton Paar WESP 502 Rotary Rheometer equipped with a Powder Cell; b) photograph showing the used compression piston with an exchangeable plate.

The preconditioning of the powder sample is done by fluidisation and optionally stirring (for cohesive powders) to achieve similar initial conditions for every test run. The fluidisation is done using filtered and dried compressed air. The air is dried to guarantee a dew point of -20 °C. The fluidisation by air with a fixed humidity also reduces the influence of the ambient air humidity. The air flow is controlled by a mass flow controller allowing a volumetric flow rate of 0-5 Nl/min.

As the compressibility β was already provided by Sandra Stranzinger (using an FT4 Powder Rheometer®), only the confined load stiffness and the confined unload stiffness were analysed using this setup. The compressibility is stated in section *2.7.5* in Table 4.

The definitions of these metrics are provided by Eq. (31)-(33). With h_0 being the initial bed height, h_1 the height of the compressed bed, h_2 the height of the unloaded bed, h_3 the height of the partially loaded bed and h_5 the height of the partially unloaded bed. The indices of σ are defined respectively.

$$\beta = \frac{h_0 - h_1}{h_0} \tag{31}$$

$$k_{load} = \frac{(\sigma_3 - \sigma_2)\, h_1}{h_3 - h_2} \tag{32}$$

$$k_{unload} = \frac{(\sigma_5 - \sigma_1)\, h_1}{h_5 - h_1} \tag{33}$$

For the simulation of this test the initial packing is used as restart point. The powder bed is placed in a cylindrical container and compressed by a piston. The movement of this piston is controlled by a PID-controller-model. The input parameters for this model are the desired normal force, the maximal traveling speed of the piston and a proportional controller constant. After the first compression to a normal stress of 15 kPa, the stress is lowered to 0.5 kPa and therefore the bed expands. Afterwards the stress is again increased to 15 kPa. The cycle of unloading and reloading is done five times. After the last reloading step, the normal stress is reduced close to zero. The powder bed as conditioned by this test is used as restart point for a tensile strength test. The powder bed going through different stages of the confined compression test is shown in Figure 7. The stages are: a) initial packing, b) during first compression, c) compressed by 15 kPa, d) unloaded to 0.5 kPa. The colour indicates the force magnitude acting on the particles.

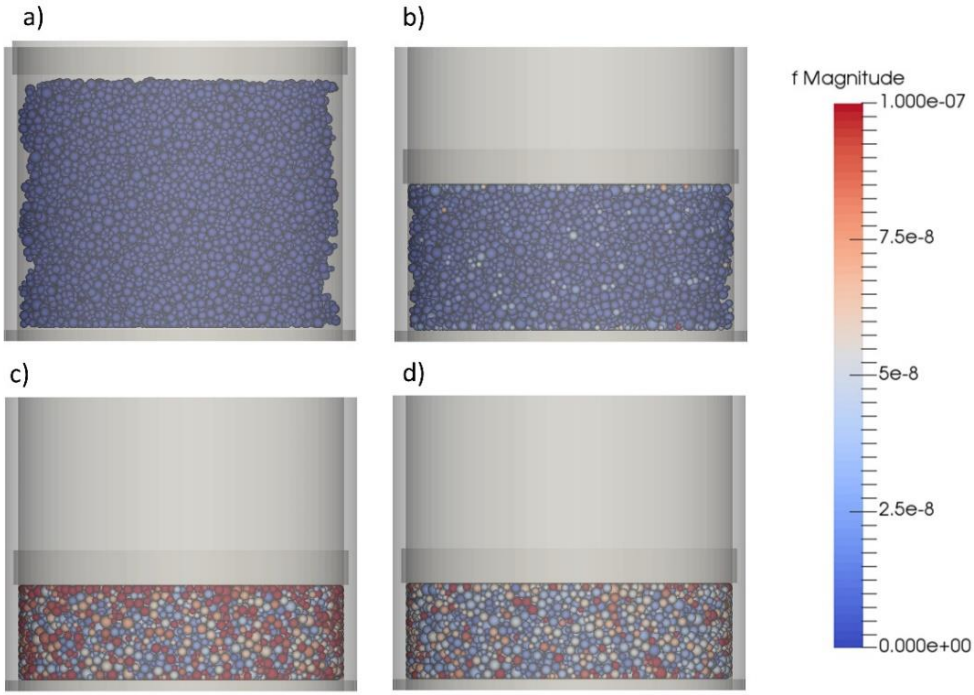

Figure 7: Compression and unloading of a cohesive powder bed. a) uncompressed initial packing; b) bed during compression; c) bed compressed by the specified maximal normal load; d) bed unloaded to the reduced load. Colour indicating the force magnitude acting on the particles

As can be seen the compression piston overlaps with the container, this is to prevent escape of the particles. Since contact forces are only calculated for particle-wall and not for wall-wall interactions, this does not influence the results. For high local particle-wall forces it can happen that the overlap exceeds plausible values leading to the escape of particles form the bed. To prevent this the particle-wall contact stiffness $k_{1,wall}$ is set to the 30-fold value of the interparticle contact stiffness k_1. This relation was determined empirically.

An exemplary stress-strain diagram using the introduced nomenclature is provided in Figure 8 a) showing experimental results and b) showing results of an uncalibrated simulation. The strain shown in the diagrams is defined by $(h-h_1)/h_1$. An obvious difference between experiment and simulation can be observed regarding the curve shape as the real powder exhibits a change of the strain for constant stress, which is not observed to this extend in simulation. This is due to rearrangement processes which are more present in the real powder. For calibration an arithmetic mean for the applied load cycles is calculated to gain a single value for load-stiffness and unload-stiffness.

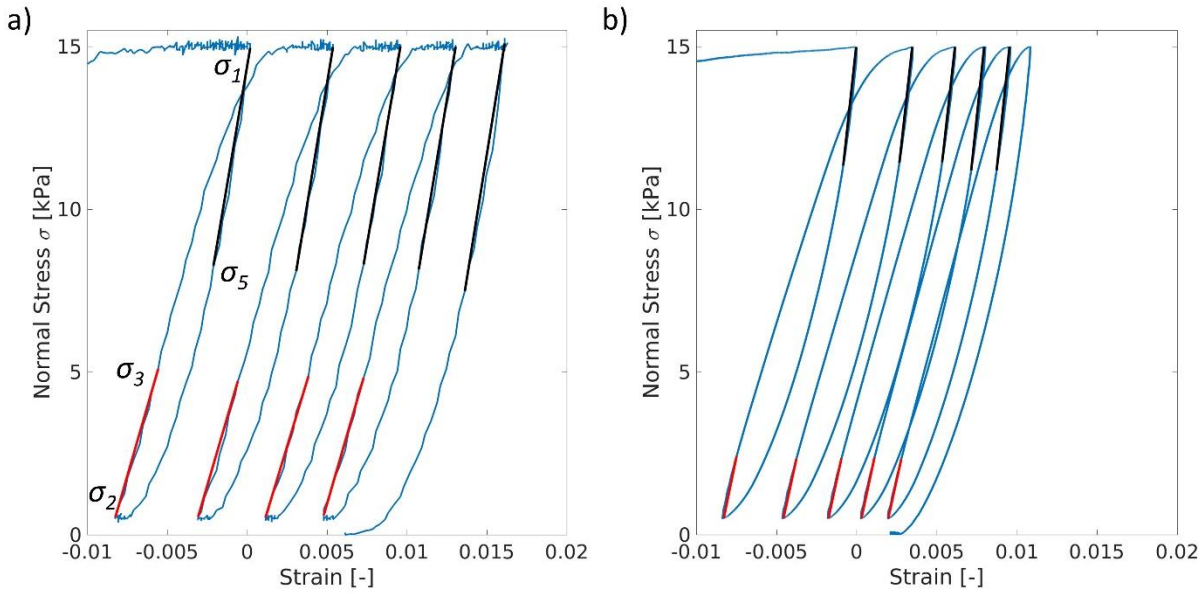

Figure 8: Stress strain diagrams the confined compression test. a) diagram resulting from experiment; b) diagram resulting from uncalibrated simulation

2.7.3 Tensile Strength Test

To receive further information about the cohesive properties a tensile strength test is done. Since this metric should be predominantly affected by the Hamaker constant, the cohesion stiffness k_c and the unloading stiffness k_2 it is suspected to be a good metric for the calibration of these parameters.

The real experiment is conducted as described by (Schweiger & Zimmermann 1998). In this approach a moderately to highly viscous fluid is deposited on the compression piston's surface, facing the sample. In the present work a standard viscosity sample called AW2000 (supplied by ZMK-Analytik-GmbH, Bitterfeld-Wolfen, Germany), having a dynamic viscosity of 1 Pas at 20°C, was used. This fluid leads to sufficient adhesion between piston and powder, to retain the contact created in compression. After the desired compression stress is achieved, the moving direction is inverted. Measuring the force needed to pull off the piston, one can determine the tensile strength of powder compacts, which were created with low consolidation stress. This experiment is realised with the same setup as the confined compression test, except for the piston. Since the pistons surface is covered by a liquid, a non-porous stainless-steel plate is used. For the low compression speed used, the annular gap between the piston and the glass tube provides a sufficient cross section for ventilation. After the test execution the fracture surface should be

examined to be sure if the fracture occurred inside the powder compact and not on the interface between powder and piston. The photograph provided in Figure 9 indicates a fracture within the powder compact, since the piston is covered with a compacted powder layer (except for the marked area).

Figure 9: Photograph showing the fracture surface, created by a tensile test according to (Schweiger & Zimmermann 1998) .

In simulation the test is realised by loading the pre-compressed powder as well as the piston at its last position from the confined compression test. For this test the cohesion parameters, i.e. the Hamaker constant and the cohesion stiffness, between piston and powder as well as between bottom and powder are adapted as stated in the empirical determined equations (34) and (35).

$$A_{H,wall} = A_H \left(10 + \frac{90\ (r_{real} - 5)}{45}\right) \tag{34}$$

$$k_{2,wall} = k_2 \left(10 + \frac{5\ (r_{real} - 5)}{45}\right) \tag{35}$$

Additionally, a frictionless cylindrical wall is used, which surrounds, and therefore stabilises, the powder sample without influencing the test result. The parameters determining the cohesion are set to zero for the contact between the cylindrical wall and the particles. While Figure 10 a) shows the simulation setup at the starting point of the simulation run, Figure 10 b) shows the fractured powder bed. As this indicates, the weight of powder, sticking to the piston has to be taken into account. The high force magnitudes at the contact area with the piston and the bottom are due to the increased cohesion for the particle-wall contacts.

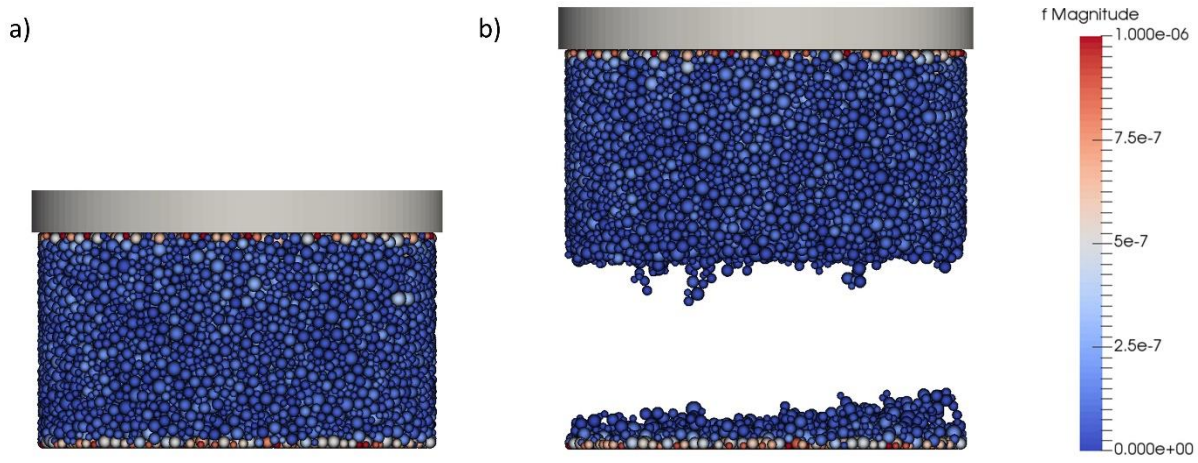

Figure 10: Simulation setup of the tensile test. Bottom and cylindrical wall are not shown. a) shows the starting point of the simulation; b) fractured powder bed. Particles coloured by the force magnitude [N] acting on them.

In Figure 11 exemplary stress-strain diagrams are provided to illustrate, how the tensile strength is determined from the results. As can be seen, there are some fundamental differences between the results from experiment (Figure 11 a) and from numerical simulation (Figure 11 b). One can see, that the fracture occurs at a lower strain in the experiment, furthermore the fracture is more abrupt, meaning that after exceeding the tensile strength a fast increase in normal stress can be observed. In simulation the tensile strength can also be determined, but the fracture behaviour is different, as the particle contacts break slowly across the bed.

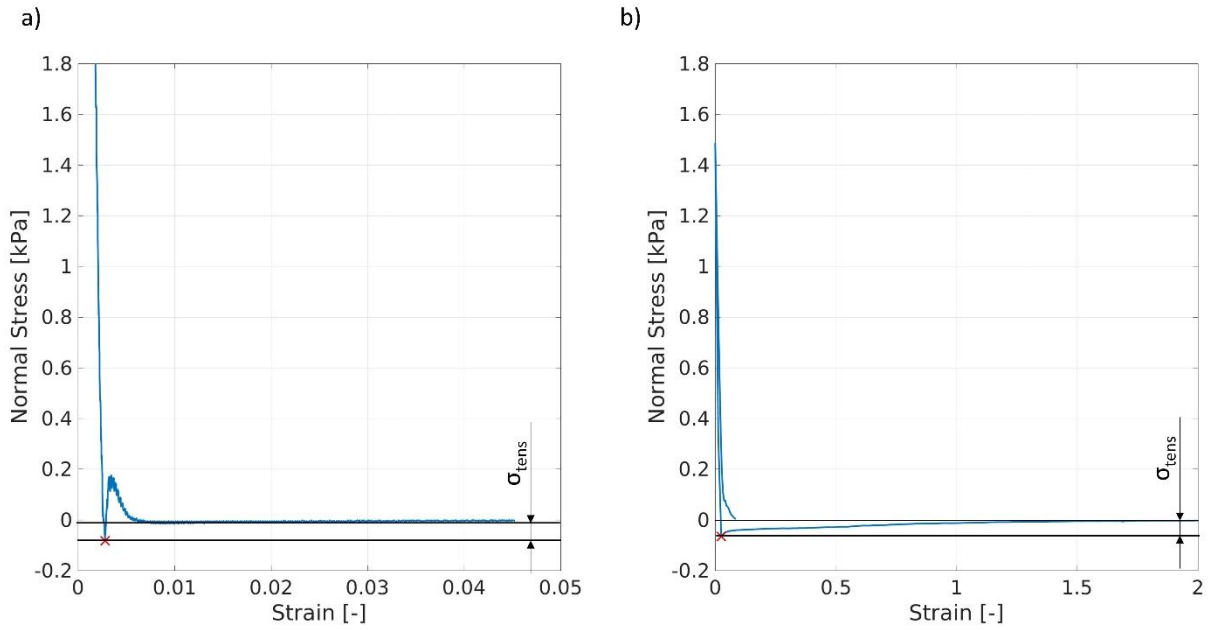

Figure 11: Stress-strain diagrams of tensile tests. Red cross marking the point of fracture. a) results from experiment; b) results from numerical simulation

Also chains of particles are present (Figure 10 b). Therefore, the residual weight of powder on the piston can only be determined if the strain is high enough to break all chains linking both powder-compact fragments. This breaking of chains might be the reason for the almost logarithmic progression of the normal stress after fracture in Figure 11 b.

On the other hand, for the experiment it is important to determine the residual weight as soon as possible, since agglomerates which were sticking to the upper fragment directly after fracture might fall off. This can be observed in Figure 11 a) as the normal stress approaches zero for higher strains.

2.7.4 Rotational Shear Test

Since the real shear test is executed with a FT4 Powder Rheometer® according to the standard shear test experimental definition by Freeman Technology, this test was also rebuilt in the simulation. In this test the powder, which is preconditioned by a stirrer, is compressed, by a pre-defined normal load σ_{pre} (in the present work 3 kPa), and pre-sheared by the shear head. The shear head is equipped with vanes preventing particle slip. The rotational speed is limited to 0.05 min^{-1} to supress dynamic effects. The torque and normal force acting on the powder are recorded by the measuring device. As the powder is compressed during the pre-shear step the acting torque, i.e. the shear stress increases. The powder is sheared until the shear stress reaches a constant value. This value is called pre-shear stress subsequently. After pre-shearing the acting torque is reduced to zero and the normal stress is reduced to a specified value σ_x. Then the torque is again increased until yield stress τ_1 is reached leading to a fracture of the compressed bed. This fracture may be indicated by a sudden decrease of the torque signal or simply by a constant torque signal. The characteristics of this fracture behaviour are dependent on the powder properties and the ratio of σ_{pre}/σ_x. This procedure of pre-shear and shear test is repeated for different values of σ_x, stated in Table 3, yielding a collection of data points. A linear regression of the results for different normal stresses is done, resulting in the so-called yield-locus, characterised by the slope k_{YL} and the intercept τ_0. A diagram showing pre-shear point, yield points and the yield locus is provided in Figure 12.

Table 3: Normal stress combinations used in the rotational shear test

σ_{pre} [kPa]	3	3	3	3	3
σ_x [kPa]	2	1.75	1.5	1.25	1

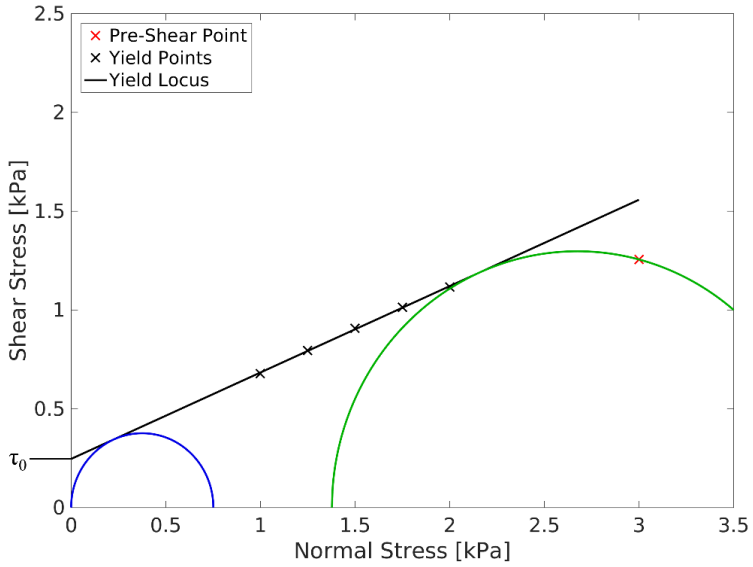

Figure 12: Stress diagram showing the results of a shear test

In simulation this test is modelled using two simulations. One for the pre-shear step and a second one for the shear step. In the first simulation the bed is compressed and pre-sheared applying a constant rotational speed as in the real experiment. One difference between simulation and experiment is, that in the simulation the container is moved to apply the normal stress. This is done, since the software does only allow one movement mode for one geometry (i.e. a mesh-file). As the shear head already does a constant rotational movement, the force controlled translational movement has to be done by the container. The inertial effects of the moving powder bed can be neglected, since the displacement in the compressed state, which is relevant for the measurement of the pre-shear stress is in the order of single particle diameters. The duration of the test is set high enough for the simulation to reach a stationary shear stress.

The powder bed as well as the shear-head-mesh and the container-mesh at their latest position are stored as restart files for the shear test simulation. For the determination of the yield locus the simulation is started with the normal stresses σ_x as stated in Table 3, using the same restart files for every run. To determine the yield stress, the shear head is now torque controlled. This means, that instead of a constant rotational speed, a specific torque is defined, which should be achieved. This

value is set to a value above expected shear resistance. The proportional constant of the controller needs to be adjusted to a value which allows for a fast and stable simulation. A sufficient time resolution can be achieved by a high number of data points or by a low maximal rotational speed. The maximal rotational speed must be set low enough to be sure, that it has no influence on the yield stress. To ensure this, a variation of this speed around the used value was done. As the simulations with different rotational speeds yielded the same results, the selected speed was considered fitting.

The execution of the shear experiments was not part of the present thesis. The experimental results which are needed for calibration were provided by Sandra Stranzinger and are stated in Table 4 together with other results from other test which were used for calibration but not executed by the author of the present thesis.

2.7.5 Wall Friction Test

Experimentally the wall friction test is done using the FT4 Powder Rheometer® in combination with a compression piston with exchangeable plate. This allows to vary the wall material, the wall-particle friction angle is determined for. To do so the preconditioned powder is compressed by increasing normal stresses. After a specified stress value is reached, the piston rotates while the normal stress is kept constant. The required torque for rotation at the specified normal stresses is recorded to calculate a shear stress. For the recorded values-pairs of normal and shear stress a linear regression without intercept is done. The slope of the linear function determines the wall friction angle. The experimental values are also stated in Table 4

The numerical simulation was done with the same geometrical setup as the confined compression test. The difference is that the normal stress is now applied by the container, as for the shear tests. The rotation is done by the compressing piston. The test sequence is defined in the same way as the real experiment: compression, followed by rotation under constant normal stress. The torque signal is recorded for the normal stresses 1, 1.25, 1.5, 1.75, 2 and 3 kPa.

Table 4: Experimental results for test executed by Sandra Stranzinger

	Compressibility [%]	Wall Friction Angle [°]	Pre-Shear Stress [kPa]	Yield Locus [kPa]
LH100	5.73	7.77	1.67	$0.608\ \sigma + 0.14$
LH220	46.29	20.03	2.88	$0.796\ \sigma + 0.88$

2.7.6 Hopper Discharge

As mentioned in the introduction the applicability of the powder model created by the calibration procedure shall be tested by modelling a hopper discharge with the same powder model parameters. To do so a wedge shaped hopper providing mass flow is designed based on the simulation results of the shear test according to the design process described in (Schulze 2009). The designed hopper is then modelled by its side walls. To reduce the computational effort only a slice of the hopper is simulated. The open front and back are defined to be periodic boundaries. The simulation is then at first analysed qualitatively, in a visualisation software, to determine if the mass flow is achieved or not.

The simulation process consists of the creation of an initial packing, similar to that described in 2.7.1, within the hopper with closed discharge gate. After the settling of the powder the discharge gate is opened (the closing wall is removed in simulation). Figure 13 Depicts the steps of the simulation, i.e. a) particle insertion, b) settled powder bed, c) acceleration after opening the discharge gate and d) powder leaving the hopper in mass flow.

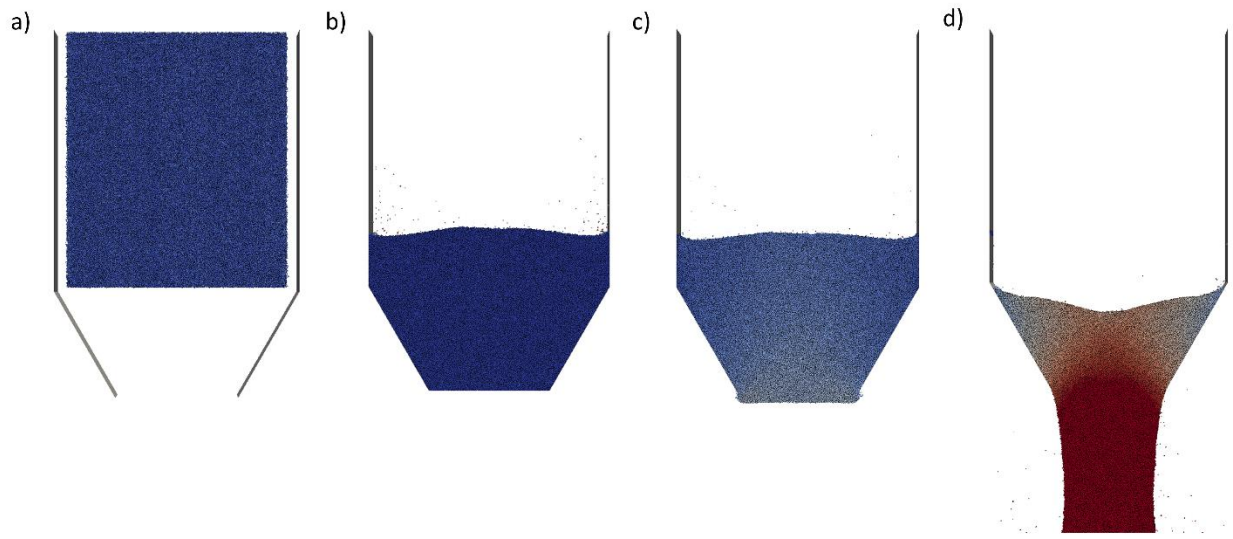

Figure 13:Simulation procedure for hopper discharge simulation. a) insertion of particle; b) settled powder bed; c) acceleration of the powder bed after discharge gate opening; d) mass flow of powder; particles coloured by speed

3 Results and discussion

This section will present the results of simulation as well as those of the executed experiments. Before coming to the results of the different test setups and of the DoE, the results of different possibilities for the creation of an initial packing will be discussed.

3.1 Initial packing creation

Four ways of generating an adequate powder bed for simulation were tested. The aim was to investigate the impact of the method on the influence of particle size on the solid-fraction of the created packing. Figure 14 shows a plot of the solid fraction over the particle diameter for different approaches of creating a realistic initial packing as well as experimental results for glass beads and the values provided for LH100 and LH220. The results show a good qualitative correlation between the Van der Waals (VdW) approach and experimental values determined by (Parteli et al. 2014) for glass beads. Especially the strong decrease for small particle diameters can be modelled well by the VdW-approach. This is due to the fact, that not only the contact stability increases for smaller particles (as for all other approaches) but also the contact promotion also increases due to an increasing ratio of the attracting force to particle inertia. Furthermore, as the particle size decreases, the relative active range of the VdW-interactions increases. For the smallest investigated particles, the VdW-cut off distance is in the same order of magnitude as the particle diameter.

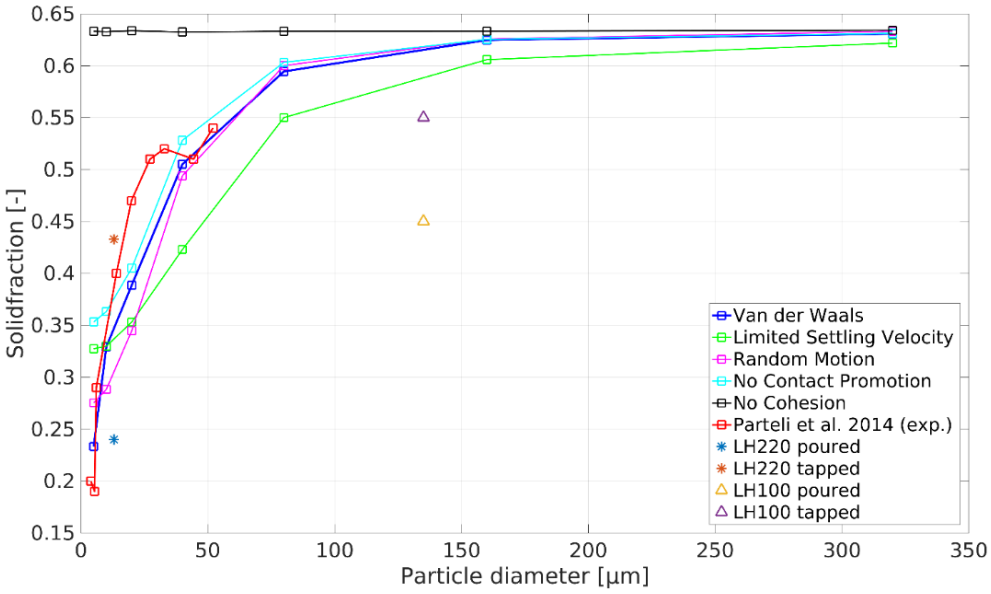

Figure 14: Solid fraction over particle diameter for different approaches to create an initial packing

These results suggest that the VdW approach is the best option to generate realistic initial packings, for a simple DEM approach which does not account for the surrounding fluid.

For comparison, also initial packings without any cohesion are created. The stars and triangles mark the poured and tapped density of the two Lactohale® powders which are to be modelled later on. While the values for Lactohale® 220 (LH220) correlate with the experimental results for glass beads and also with those of the simulation, both solid fractions of Lactohale® 100 (LH100) are below the simulated values (for the used cohesion parameters) and do not follow the trend of the experiments for glass beads. A first intuitive way is to reason this by the particle shape – while LH100 consists of whole tomahawk shaped lactose crystals, LH220 consists of irregular shaped particles due to the milling process used to lower the particle size (DFE Pharma n.d.; DFE Pharma n.d.). Hence, one would think that the irregular shape is closer to spheres and therefore LH220 is closer to the results for glass spheres. Further literature study supports this. The high sensitive circularity[1] for the fines of LH100 is stated with 0.859 by (Kinnunen et al. 2015) for the larger particles the circularity is assumed close to that of LH200 stated with 0.56 by (Shalash et al. 2017). For LH220 the circularity is given with 0.680 (for particle size 5 – 14 µm) and with 0.878 (for particles < 5µm) by (Das et al. 2013).

3.2 Screening for important Parameters

This section will present the results of the DoE which was run with 12 varied parameters. The influence of the different parameters on the different tests is then discussed. The used parameter combinations are stated in Table 17 in the Appendix.

3.2.1 Initial Packing

Even though the relative initial packing density is not used for calibration, it is an important metric, since it has a high impact on the compressibility of the powder. In Figure 15 a main effect plot for all varied parameters is provided. As can be seen, the most important factors for this metric are the radius (r_{real}) and the Hamaker constant ($A_{H,real}$). The coefficient of static friction μ_s, Young's modulus Y_{real}, k_2/k_1, the plasticity depth ϕ_f and the coefficient of rolling friction μ_r are also assumed to influence the initial solid fraction. On the other hand, the coefficient of dynamic friction μ_s, the k_c/k_1 ratio, the k_t/k_1 ratio, the coefficient of restitution e and the γ_t/γ_n ratio seem to play a negligible role.

[1] The high sensitive circularity (HSC) is defined as the projected area times 4π over the squared projected perimeter

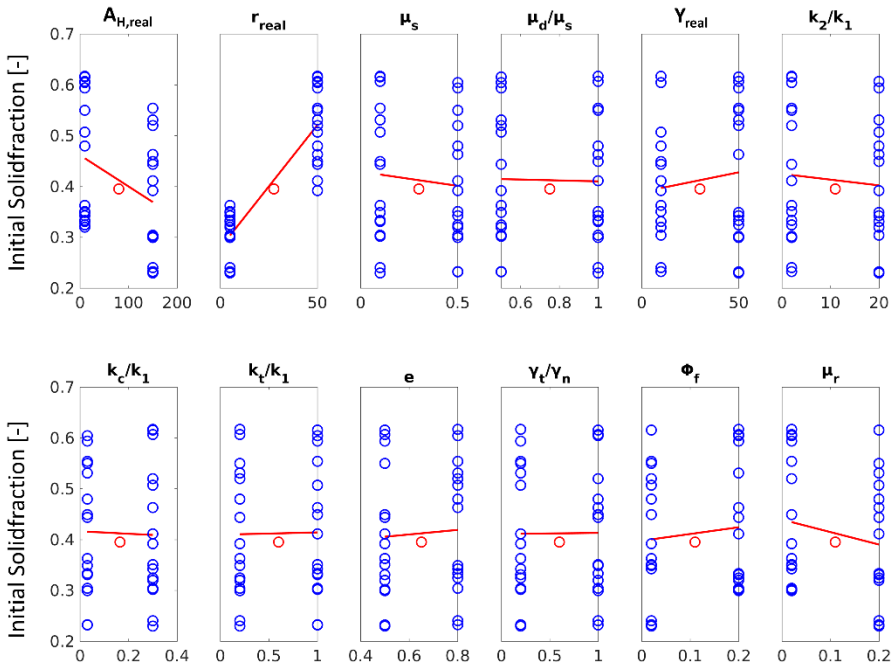

Figure 15: Main effects plot for the initial solid fraction using 12 varied parameters

3.2.2 Confined Compression Test

3.2.2.1 Experimental Results

Before the results for the simulation, i.e. the main effects for the different parameters are presented, the results of the executed experiments are presented and discussed. Figure 16 shows the results for load- and unload-stiffness for Lactohale® 100. The x-axis represents the compression cycle, the colour indicates the experiment number. As depicted in Figure 8a only 4 load cycles are done in the experimental runs. Despite the used pre-conditioning step, the measured values show a significant deviation from each other, indicating that either the test itself or the preconditioning step needs further development. Nevertheless, the values are used for calibration, as the arithmetic mean values for all load and unload stiffnesses are assumed to be still a valuable metric. The relation of load and unload stiffness is in accordance with theoretical considerations, as the unload stiffness is higher than the load stiffness. This is due to the fact that the bulk stiffness increases with compression.

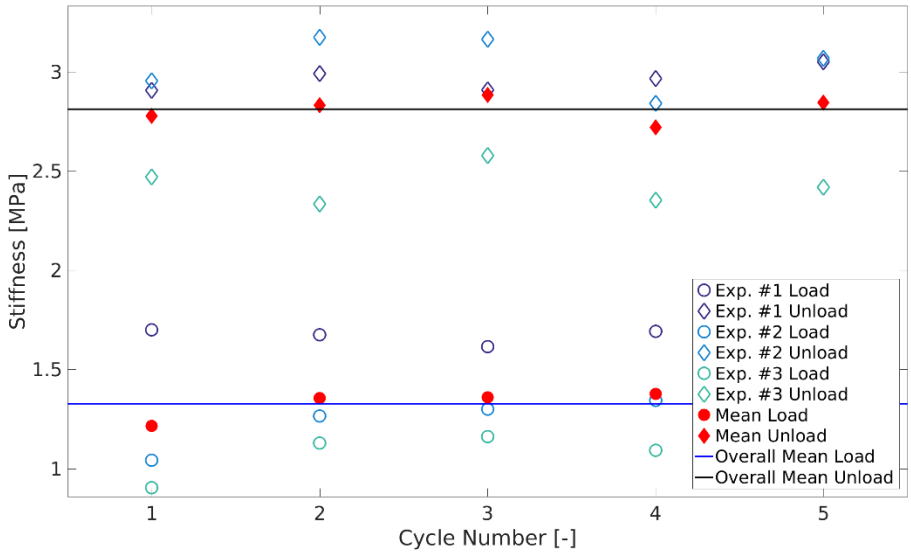

Figure 16: Diagram showing the bulk stiffness of Lactohale® 100 over the number of the compressions cycle. Unfilled symbols: single results; filled symbols arithmetic means for specific compression cycle, lines overall arithmetic means

The data for Lactohale® 220 is provided in Figure 17. For LH220 a decrease of the load stiffness with increasing number of load cycles seems observable, while this trend is interestingly not observable for the unload-stiffness. Despite the preconditioning of the cohesive powder seems more challenging, the reproducibility seems better. While for LH100 a trend for each experiment can be observed the results for LH220 seem more randomly scattered.

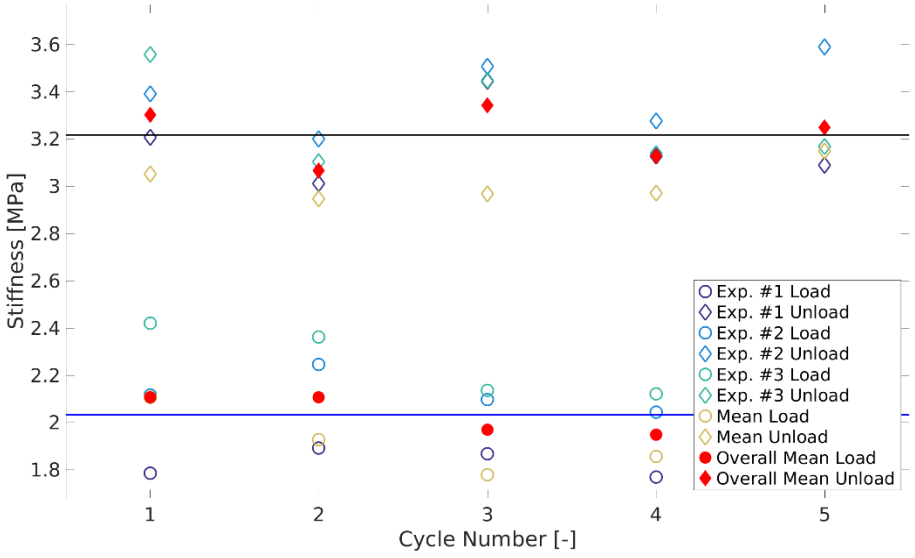

Figure 17: Diagram showing the bulk stiffness of Lactohale® 220 over the number of the compressions cycle. Unfilled symbols: single results; filled symbols arithmetic means for specific compression cycle, lines overall arithmetic means

The bulk stiffness values used for calibration, i.e. the overall means for each powder, as well as the experimental final solid fractions are stated in Table 5.

Table 5: Bulk-stiffness values and final solid fraction determined by confined compression experiments

	Load-Stiffness [MPa]	Unload-Stiffness [MPa]	Final Solid fraction [-]
LH100	1.327	2.812	~0.50
LH220	2.033	3.217	0.38

3.2.2.2 Simulation Results

The main effect plots for compressibility are provided in Figure 18. As suspected the compressibility depends strongly on the initial solid fraction. Except for the influence of the coefficient of static friction the compressibility shows the inverted behaviour of the initial solid fraction. To further investigate this relation, the final solid fraction, i.e. after compression is provided in Figure 19, which gives an explanation for the different behaviour for μ_s. According to these results the final solid fraction is almost only dependent on μ_s and the Youngs modulus. Concerning Youngs modulus the presence of overlaps has to be considered, leading to an unrealistically high packing density for rigid spheres.

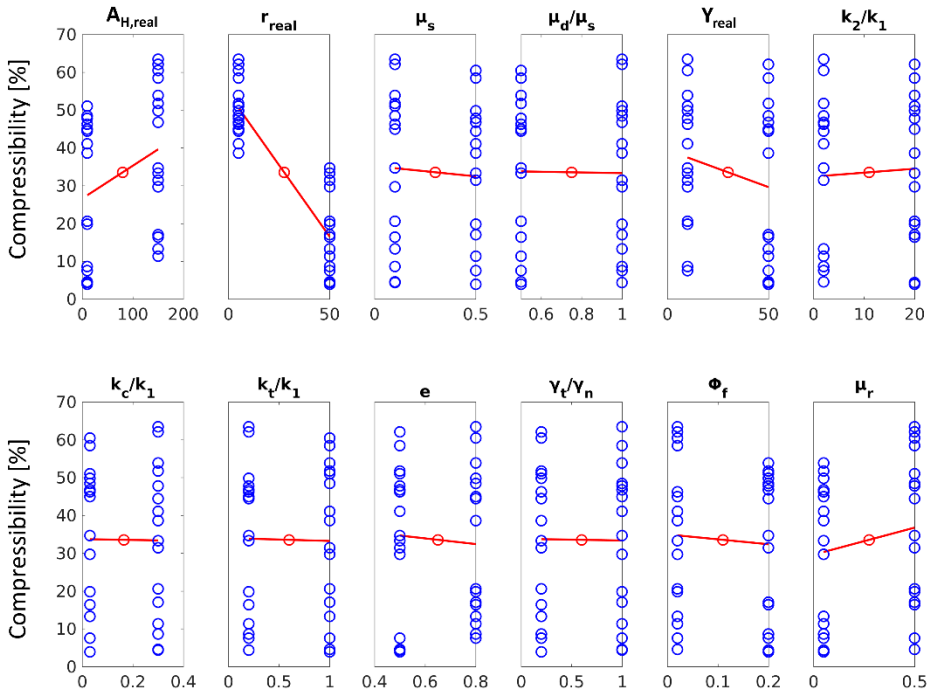

Figure 18: Main effect plots of the compressibility using 12 varied parameters

The strong dependency of the compressibility on the initial packing, and therefore powder preparation, as well as on the final solid fraction, which is strongly dependent on the particle shape, does not suggest the compressibility to be a good metric for the calibration of a model using

spherical particles. Nevertheless, it is a least considered to provide a comparison to the work of (Bramböck 2017).

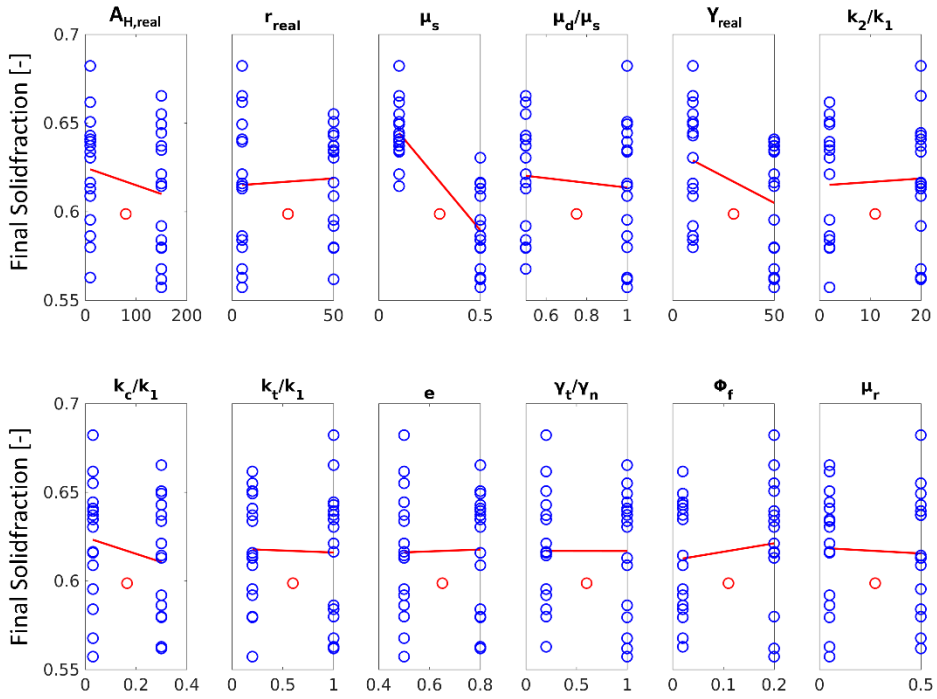

Figure 19: Main effect plots for the final solid fraction using 12 varied parameters

Figure 20 shows the main effect plots for the loading stiffness. The results are in good correlation with predictions that can be made when considering the determining characteristics of the used normal and tangential model. Obviously, the bulk stiffness increases for increasing material stiffness parameters, i.e. Young's modulus and the k_2/k_1 ratio. Also, the influence of the plasticity depth can easily be explained, as it determines the overlap at which the (particle)-loading stiffness is increased to k_2. Therefore, the bulk-stiffness increases with decreasing ϕ_f. The reason for the influence of μ_s is not that obvious. As μ_s limits the elastic tangential contact force it determines the maximum elastic tangential displacement, together with the tangential stiffness k_t. If μ_s has a high value the bed deformation is higher due to a higher tangential displacement staying available. The influence of k_t is then again similar to that of Y_{real} and k_2/k_1.

Concerning the unloading stiffness (Figure 21), same can be said for Y_{real}, k_2/k_1, ϕ_f and μ_s. The influence of r_{real} can only be reasoned by speculations not mentioned here since it might as well be the influence of confounded three-parameter interactions.

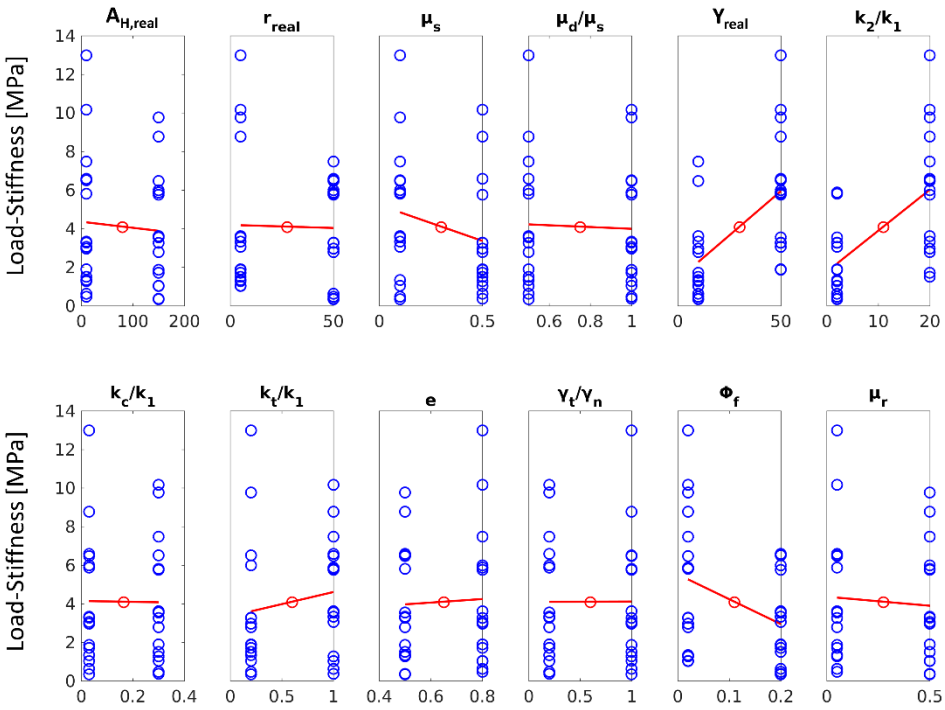

Figure 20:Main effect plots of the load-stiffness using 12 varied parameters

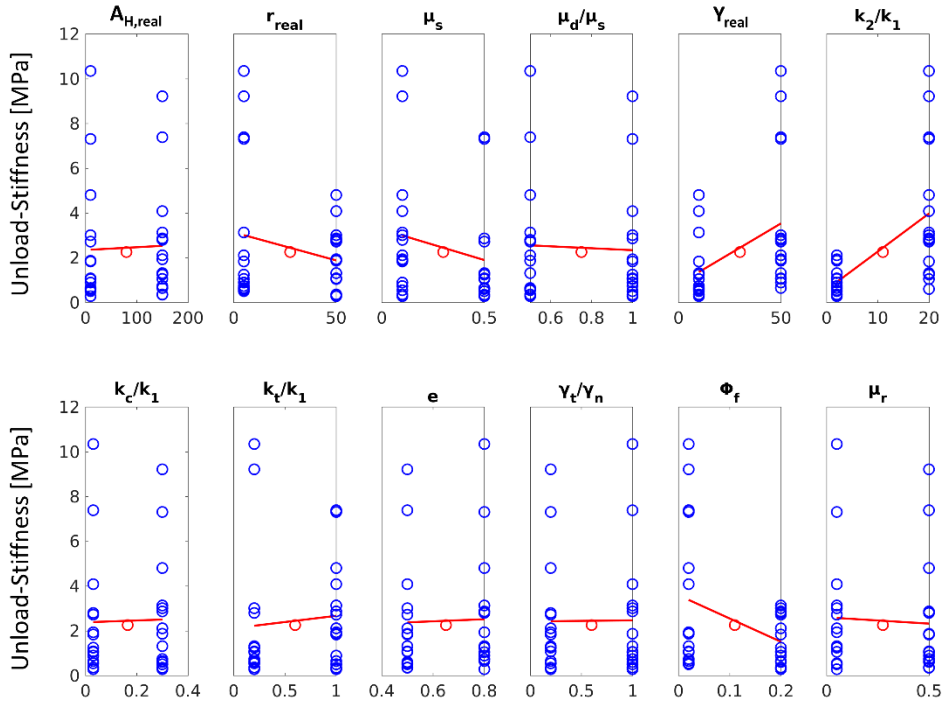

Figure 21: Main effect plots of the unload-stiffness using 12 varied parameters

3.2.3 Tensile Test

3.2.3.1 Experimental Results

The limited accessibility of the measuring setup for the tensile test made only two experimental runs for the cohesive LH220 possible. For the free-flowing LH100 it was not expected to gain any meaningful results and no test was executed. Therefore, only the results for LH220 are presented in Table 6.

Table 6: Results from experimental tensile tests

	Tensile Strength [kPa]
Experiment 1	0.0569
Experiment 2	0.0724
Value used for calibration	**0.0646**

3.2.3.2 Simulation Results

The main effect plots provided in Figure 22 show that the used model is able to model powder-compacts with (unrealistically) high tensile strength. The values measured for LH220 are within the lower part of the range. Hence the modelling of cohesion for this powder should be possible.

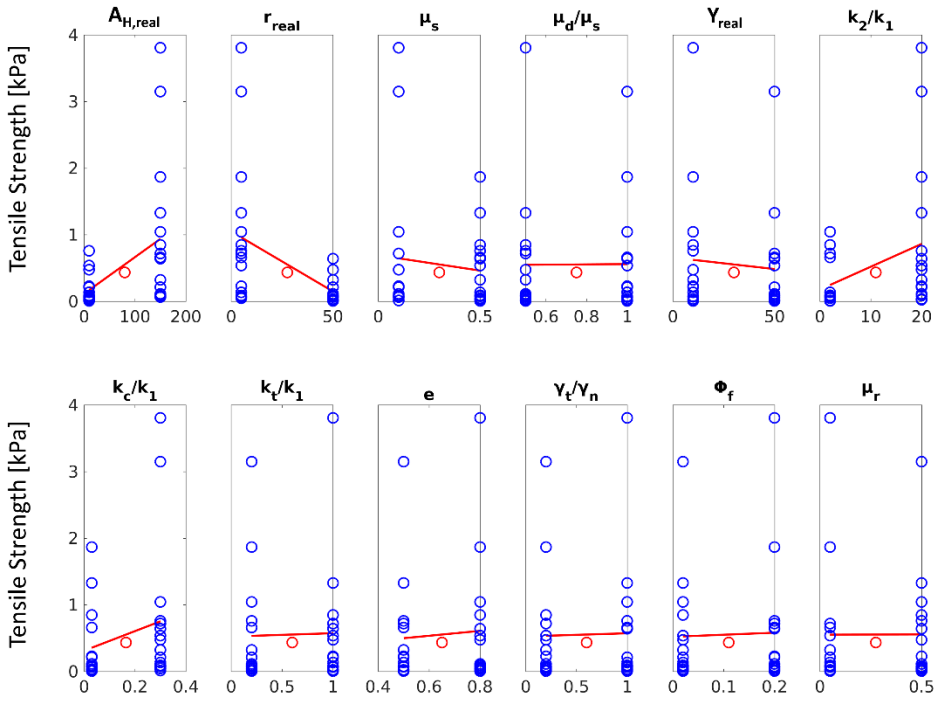

Figure 22: Main effect plots of the tensile strength using 12 varied parameters

The comparability of the measured tensile strength and the simulated one needs to be viewed critically. Even though the simulation is designed to represent the executed measurements the different solid fraction after compaction and therefore prior to the tensile test deviates strongly between experiment and simulation. As the number of contacts in the in the fracture surface plays a major role when it comes to tensile strength this deviation may have a high impact on the results.

3.2.4 Shear Test

As the execution of shear experiments was not part of the present work, only the results of numerical simulation are presented in this section. Prior to the discussion of the main effects it should be mentioned, that there were some complications, modelling the shear test. The simulations did not yield plausible results for all parameter sets. Not plausible means in this context, that the pre-shear stress and the results from the shear-tests resulting in the yield locus do not always correlate. Normally a shear test should yield a diagram like depicted in Figure 23a. The black crosses indicating the results of the shear-tests with different normal stresses and the red cross indicating the pre-shear point. The green circle should tangent the yield locus on the one hand and on the other hand the pre-shear point should be an element of the circle. As for some parameter combinations results like depicted in Figure 23b were yielded, there is no circle fulfilling both requirements. It is suspected that there is some mechanistical error or shortcoming in this simulation. The pre-shear point lying above the yield locus indicates that, the consolidation of the powder is not modelled correctly. As this error could not be resolved in a reasonable time, work was continued, since the main effects showed plausible trends.

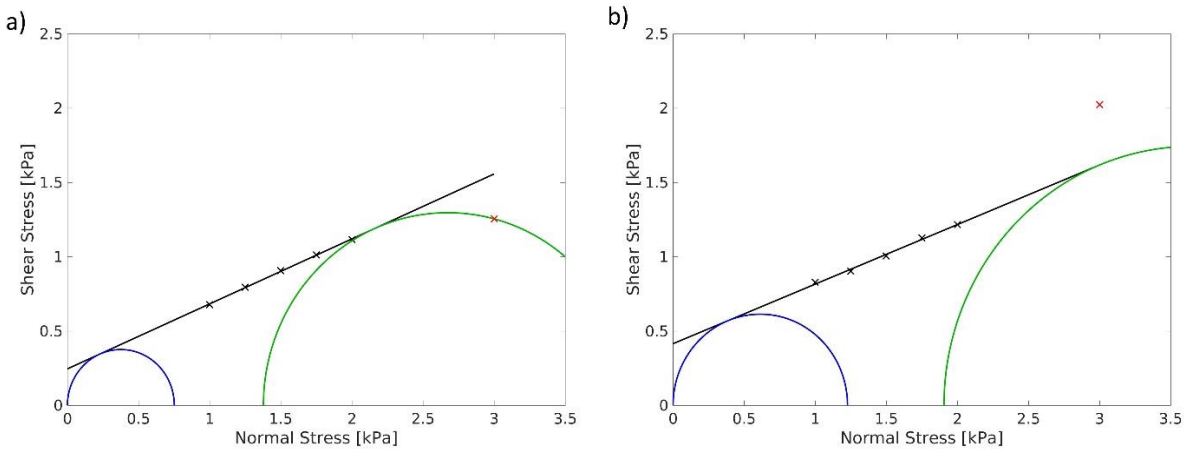

Figure 23: Diagrams showing the evaluation of shear test results; a) showing results which are describeable with the standardised evaluation procedure; b) showing non plausible correlation of pre-shear point and yield locus

3.2.4.1 Simulation Results

The main effect plots for the pre-shear test provided in Figure 24 show that the pre-shear stress is predominately influenced by the Hamaker constant, the particle radius, the k_2/k_1-ratio and the k_c/k_1-ratio. Generally, it can be said, that the same parameters, that lead to a high cohesion, when increased, lead to high pre-shear stresses. Additionally, an impact of the coefficient of static friction can be noticed, but not in the expected extend. Interestingly no effect of the coefficient of rolling friction on the pre-shear stress was observed, which is in contradiction with the results of (Ji et al. 2009) showing that the rolling friction has an important impact on the shear stress. The discrepancy might result from the use of a different rolling friction model, as (Ji et al. 2009) used a spring dashpot model limited by a Coulomb criterion also for rolling friction, in contrast to the CDT model used in the present work.

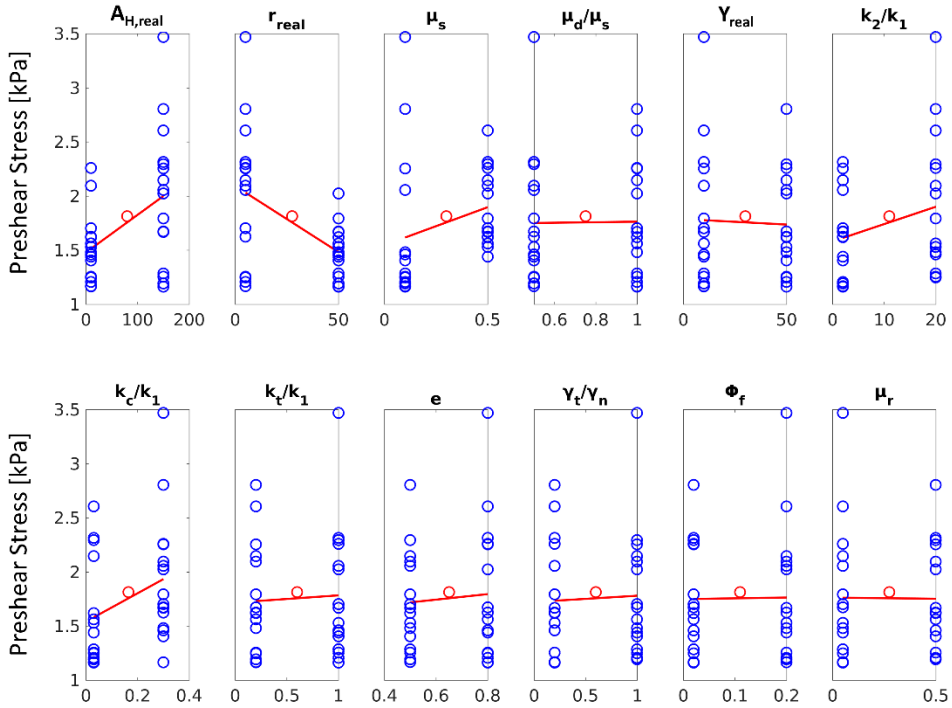

Figure 24: Main effects plot for the pre-shear stress using 12 varied parameters

As expected the main effects plot for the intercept of the yield locus, provided in Figure 25 indicate that the intercept is only dependent on cohesion and therefore on $A_{H,real}$, r_{real}, k_2/k_1 and k_c/k_1. The slope of the yield locus (Figure 26) shows also strong dependency on the cohesion, but inversely, meaning that a high cohesion leads to a low slope of the yield locus. This is plausible, since a high level of cohesion decreases the influence of external forces on the shear resistance of a powder bed.

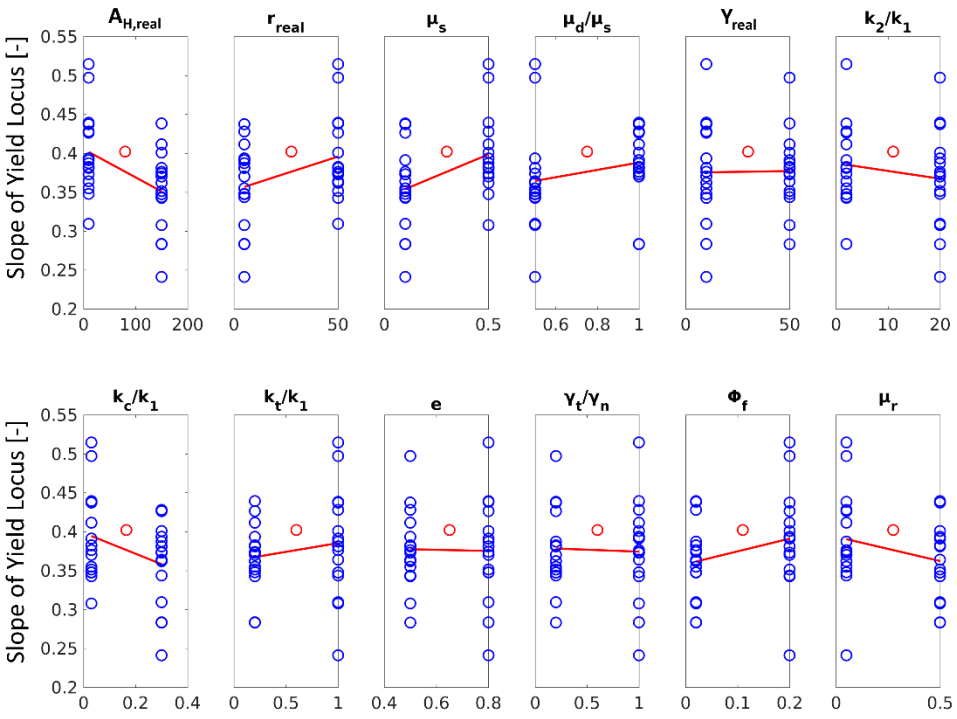

Figure 25: Main effects plot for the intercept of the yield locus using 12 varied parameters

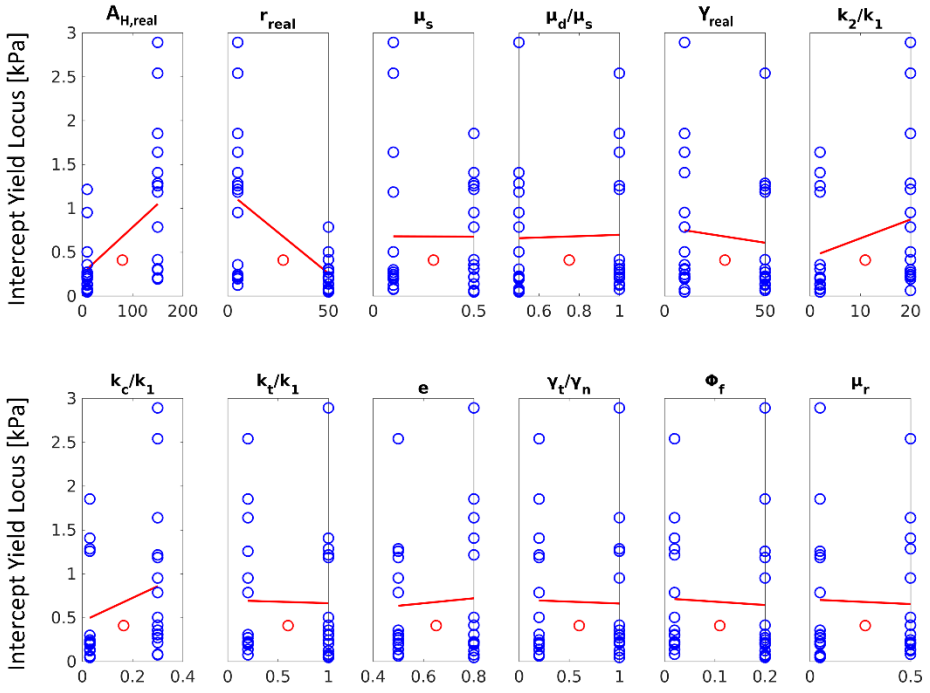

Figure 26:Main effects plot for the slope of the yield locus using 12 varied parameters

3.2.5 Summary

Overall it can be said that the variation of the damping parameters had no significant impact on any metric, same can be said for the tangential stiffness and the ratio μ_d/μ_s. Due to this and the observations reported by (Madlmeir 2018) that the modelling of the transition of static to dynamic friction shows unphysical behaviour in the implemented Luding tangential model, the ratio of μ_d/μ_s was set to 1 to in the following simulation. For e, γ_t and k_t/k_1 the mean of the used parameter range was used for the calibration. This leaves us with 8 parameters to be varied and a calibration procedure as described in 2.5.2.

3.3 Calibration of the Powder Model

For the calibration of the model for LH100 and LH220 all simulations described above were run again with a changed parameter range to gain the coefficients for the equations described in 2.5.2. The parameter range was adapted according to the effects and result ranges observed in the screening. The used parameter ranges are stated in Table 7. A detailed definition of the DoE is provided in the Appendix Table 18.

Table 7: Parameter ranges for the first run in the calibration procedure

	$A_{H,real}$	k_2/k_1	μ_{stat}	Y	ϕ_f	r_{real}	μ_r	k_c/k_1
	10^{-19} [J]	[-]	[-]	[MPa]	[-]	[µm]	[-]	[-]
high	100	20	0.5	50	0.2	50	0.3	0.3
low	10	2	1.2	10	0.02	5	0.03	0.03

3.3.1 Results for large parameter range

For the changed parameter range a differences in the main effects were observed for the pre-shear stress and the slope of the yield locus. An unexpected effect of the static coefficient of friction was observed as the pre-shear stress decreases with increasing μ_s. Furthermore, the influence of plasticity depth and cohesion stiffness is inverted compared to the results for the parameter range used in 3.2 As the results for this large parameter range laid the basis for the calibration, all main effect plots are provided in the Appendix.

Using the results of this parameter study the parameters for the calibration study for LH100 and LH220 were determined. As the reliability of the different metrics for calibration is viewed

critically by the author the optimisation of the parameters was done manually to account better for the more reliable metrics. Unfortunately, there was no parameter set which led even to a qualitative agreement of all experimentally determined values and the simulated ones. As the bulk stiffnesses, the tensile strength and the results of the shear test were assumed to be the most important and reliable criteria for calibration, the parameters were optimised to fit these metrics.

At this point it has to be mentioned, that the DoE with the large parameter range was run on a smaller system size, to save computational effort. The system size was scaled by a factor of 5/8 leading to a decrease in particle number of ~75%. To account for this the parameter range for the second calibration step (running on original scale) was set rather large, i.e. each parameter was varied to ±33%.

The parameter ranges for LH100 and LH220 are stated in Table 17.

Table 8: parameter ranges used for the calibration runs for Lactohale® 100 (LH100) and Lactohale® 220 (LH220)

	$A_{H,real}$ 10^{-19} [J]	k_2/k_1 [-]	μ_{stat} [-]	Y_{real} [MPa]	ϕ_f [-]	r_{real} [µm]	μ_r [-]	k_c/k_1 [-]
LH100								
high	66.67	10.67	1.067	33.33	0.02667	66.67	0.1333	0.1333
low	33.33	5.333	0.5333	16.67	0.01333	33.33	0.06667	0.06667
LH220								
high	66.67	21.33	0.8	37.33	0.02667	20	0.1333	0.2667
low	33.33	10.67	0.4	18.67	0.01333	10	0.06667	0.1333

Regarding the regression used for the determination of design equations a comparison was made investigating the difference in mean and maximum errors if two-parameter-interaction are considered or not. As the maximum errors have only limited meaning only the mean errors are reported in Table 9. The errors are yielded by a comparison of the simulated values and the predicted values for the corresponding parameter sets. As can be seen an improvement in prediction by the factor of 1.5 to 9 can be achieved if the interactions are taken into account.

Table 9: Mean prediction errors in % for the DoE regression with and without taking two factor interactions into account

	β	k_{load}	k_{unload}	σ_{tens}	τ_{pre}	τ_0	k_{YL}
without interactions	19.2	58.3	28.6	1232	8.69	261	6.87
with interactions	5.34	20.1	9.75	272.4	1.4	29.5	4.42

3.3.2 Calibration for Lactohale® 100

Except for the pre-shear stress and the tensile strength all important experimental values, i.e. the load- and unload stiffness as well as the slope and intercept of the yield locus, were in the range of the simulated results. The range of the results as well as the experimental values are provided in Table 10.

Table 10: Range of results simulated in the calibration run and experimental results for Lactohale® 100

	β [%]	k_{load} [MPa]	k_{unload} [MPa]	σ_{tens} [kPa]	τ_{pre} [kPa]	τ_0 [kPa]	k_{YL} [-]
min	5.56	0.904	2.09	0.0739	1.75	0.14	0.487
max	33.96	3.33	6.09	0.376	2.25	0.448	0.611
exp.	5.73	1.327	2.81	0	1.67	0.14	0.608

Given this results a second optimisation of parameters was done. Again, it was not possible to find a parameter set leading to a good agreement between experiment and simulation for all metrics, if the parameters are limited to the analysed range. The final parameter set is stated in Table 11.

Table 11: Calibrated parameters used for the simulation of Lactohale® 100

$A_{H,real}$ 10^{-19} [J]	k_2/k_1 [-]	μ_{stat} [-]	Y_{real} [MPa]	ϕ_f [-]	r_{real} [µm]	μ_r [-]	k_c/k_1 [-]
33.33	5.33	0.7	17	0.0133	66.67	0.1	0.0667

In Table 12 the values predicted by the design equations, the simulated results and the deviations between final simulated values and the prediction as well as between simulation and the experiments are provided. As can be seen there are significant deviations between the simulated

values and the experimental ones. For a further improvement a change of the parameter range would be required. As the findings indicate that the systematic differences between model and real powder make a correct description with this model impossible no run with new parameter ranges was started. Even though the prediction quality on the parameter borders is improved by narrowing the parameter range compared to 3.3.1 as can be seen in Table 19 in the Appendix there are still significant deviations between prediction and simulation, if the parameters are not close to the borders used in the DoE. These deviations suggest further narrowing of the parameter range or the use of a DoE model with more than two levels to account for non-linearity.

Table 12: Predicted and simulated results as well as deviations between prediction and simulation and deviation between experiments and simulation Lactohale® 100

	β [%]	k_{load} [MPa]	k_{unload} [MPa]	σ_{tens} [kPa]	τ_{pre} [kPa]	τ_0 [kPa]	k_{YL} [-]
Predicted	11.41	1.27	2.93	0.0852	1.91	0.184	0.586
Simulated	11.51	1.12	2.76	0.068	1.95	0.214	0.559
ε_{pred} [%]	0.88	-11.81	-5.80	-20.19	2.09	16.30	-4.61
Experiment	5.73	1.327	2.812	0	1.67	0.14	0.608
ε_{exp} [%]	100.87	-15.60	-1.85	-	16.77	52.86	-8.06

3.3.3 Calibration for Lactohale® 220

The only metrics which were within the range of the simulated results were the bulk stiffnesses and the intercept of the yield locus. As no significant improvement was expected, no run with a different parameter range was started. The range of the results as well as the experimental values are provided in Table 13

Table 13: Range of results simulated in the calibration run and experimental results for Lactohale® 220

	β [%]	k_{load} [MPa]	k_{unload} [MPa]	σ_{tens} [kPa]	τ_{pre} [kPa]	τ_0 [kPa]	k_{YL} [-]
min	31.6	1.44	2.57	0.279	2.00	0.0985	0.383
max	41.7	5.80	7.98	1.49	2.60	0.969	0.600
Experimental	46.3	2.03	3.22	0.065	2.88	0.880	0.796

Despite the fact that most experimental values are not within the range simulated with the used parameter range, a final set of parameters was determined to achieve the best description of the real powder. The final parameter set is stated in Table 14. For the sake of completeness, the prediction errors on the parameter borders for this parameter range are stated in Table 20 in the Appendix.

Table 14: Calibrated parameters used for the simulation of Lactohale® 220

$A_{H,real}$	k_2/k_1	μ_{stat}	Y_{real}	ϕ_f	r_{real}	μ_r	k_c/k_1
10^{-19} [J]	[-]	[-]	[MPa]	[-]	[µm]	[-]	[-]
50	12	0.6	21	0.0267	10	0.1	0.2667

In Table 15 the values predicted by the design equations, the simulated results and the deviations between final simulated values and the prediction as well as between simulation and the experiments are provided. The results show better agreement between prediction and simulation than for LH100. The agreement between experimental data and simulation is good for the bulk stiffness. While the deviations for the shear test and the compressibility stay below 40 % the tensile strength is off by a factor of 16. This is due to the problems in modelling shear resistance, already described in 3.2.3 and 3.2.4 which is also addressed in the "Conclusions and Outlook" section.

Table 15: Predicted and simulated results as well as deviations between prediction and simulation and deviation between experiments and simulation for Lactohale® 220

	β	k_{load}	k_{unload}	σ_{tens}	τ_{pre}	τ_0	k_{YL}
	[%]	[MPa]	[MPa]	[kPa]	[kPa]	[kPa]	[-]
Predicted	38.7	2.00	3.26	0.938	2.39	0.763	0.457
Simulated	38.2	2.07	3.37	1.12	2.39	0.68	0.491
ε_{pred} [%]	-1.29	3.50	3.37	19.40	0.00	-10.88	7.44
Experimental	46.3	2.03	3.22	0.065	2.88	0.880	0.796
ε_{exp} [%]	-17.49	1.97	4.66	1623	-17.01	-22.73	-38.32

3.3.4 Calibration of the Wall Friction Angle

As the wall friction angle is suspected to have a linear dependency on the particle-wall coefficient of friction, the calibration of this metric was excluded in the procedure above. To achieve a correct

value a two-point calibration was carried out. The final values for the friction coefficient were the determined by linear interpolation.

The used parameter borders and the final coefficient as well as the corresponding wall friction angles φ_x for LH100 and LH220 are stated in Table 16 (the values in the brackets are the experimental results). The results show a strong dependency on the friction coefficient. As the result for LH100 shows, the relation is not completely linear, therefore an iterative calibration is required, but not executed within the present thesis. The good agreement for LH220 may be due to the smaller variation of $\mu_{s,wall}$.

Table 16:Friction coefficients and corresponding results for the wall friction angle of Lactohale®100 (LH100) and Lactohale® 220 (LH220); experimental results in brackets

LH100			
$\mu_{s,wall}$ [-]	0.2	0.1	0.111
φ_x [°]	12.7	6.42	7.1 *(7.77)*
LH220			
$\mu_{s,wall}$ [-]	0.2	0.15	0.18
φ_x [°]	22.4	16.48	19.9 *(20.03)*

3.4 Hopper Discharge Simulation

As described in 3.3 it was not possible to achieve a good quantitative agreement of the powder model and the real powders. Nevertheless, a hopper discharge was modelled with a selected parameter set. The design process for this parameter set yielded a maximum hopper half angle of 35° and a minimal width for the discharge opening of 0.1 m. The parameter set as well as the simulation results of the modelled powder are provided in Table 21 and Table 22 in the Appendix.

The results show that the behaviour of the powder in hopper discharge and in the shear test does not correspond as arching prevents any powder outflow even if the discharge opening is enlarged to the twice width. It is suspected that this is since the simulated shear test is not capable of depicting the correct confinement and internal friction behaviour of the powder. As also indicated by the tensile strength the modelled powders are far more cohesive than indicated by the shear test. Furthermore, the stress level in the shear test is higher than in the hopper. Therefore, powder inherent cohesive forces may be underpredicted depending on the chosen normal stresses used in the shear tests.

4 Conclusions and Outlook

The results suggest that the modelling of polydisperse powders consisting of non-spherical particles is not feasible with the chosen approach. This is indicated by the fact that it was not possible to satisfy all calibration criteria with one set of parameters and furthermore by the discrepancy between shear test results and the hopper discharge simulation. The main problem is suspected to be the particle shape. In this approach the deviation of the particle shape from a sphere is modelled by high coefficients for static, dynamic and rolling friction. Even though this may work to a certain extend as described by (Ji et al. 2009), systematic problems were observed in the present thesis. When increased to high values (0.8 -1.2) the effect of the coefficient of static friction contradicts expectations based on physical relations, i.e. an increase of the static friction coefficient leads to a decrease of the pre-shear stress. The increase of the rolling friction leads to stability issues, for the used rolling friction model, furthermore the desired effect of rolling friction on shear behaviour was not observed. As discussed in 3.1 the powders also show a different particle shape for different particle diameters, which is not considered in the present work as it would lead to a very high complexity of the powder model. In addition to the flow behaviour, also the compaction behaviour of a powder is affected by particle shape, especially the final solid fraction after uniaxial compression. While for non-spherical particles the rearrangement is only possible if also shear is induced, spherical particles can relatively easy rearrange under uniaxial pressure. Therefore, the final solid fraction is modelled far too high for the cohesive Lactohale® 220 and still too high for the free-flowing Lactohale® 100. As described in 3.2.3 this may partly explain the deviation between the measured and simulated tensile strength, as it is affected by the number of contacts in the fracture surface. The second influence on this is of course the cohesion itself which is modelled by the Hamaker constant and the cohesion stiffness. As the modelling of shear resistance due to particle shape is not sufficient using only friction and rolling resistance, the cohesion parameters need to be set to high values to overcome this weakness. This leads to an overestimation of the tensile strength and therefore to different arching behaviour than predicted by the shear test alone. This is observed when comparing shear test simulations and hopper discharge simulation.

The fact that the parameters accounting for dynamic behaviour of the particles, i.e. the damping constants, had almost no influence on the metrics used for calibration indicates, that this calibration would be only useful for quasistatic processes, such as compaction or dosing. Application to dynamic processes needs to be tested in future investigation if a model for correct static results is

found. As the particle concentration is high in all experiments, the applicability to dilute granular flows would also require further investigation.

The first step for future investigation on this topic should be the use of non-spherical particles for simulations. A framework for this is provided with the LIGGGHTS® Public version 3.8 with the introduction of superquadric particles. This approach allows for example the use of hexagonal bodies with different edge sharpness and aspect ratios. As stated by (Soltanbeigi et al. 2018) the simulation time increases by a factor of approximately 10 compared to spheres. In contrast to the use of multisphere particles, which are commonly used to model non-spherictiy, the simulation time stays nearly constant for superquadric particles if changing the edge sharpness. The use of more realistic particle shapes should reduce the need for modelling with unrealistically high friction coefficient and therefore resolve stability issues and systematic errors caused by them.

The investigations on non-spherical particles could in a first step be done using a less complex contact model, to reduce the number of parameters and focus on particle shape.

The use of different experiments/metrics for calibration should also be investigated, especially metrics accounting for dynamic behaviour.

Regarding the used DoE approach for calibration it can be said, that it is useful for the screening for important parameters and still for the calibration itself. Nevertheless, the method has significant shortcomings, in case of non-linear influences of parameters on the metrics. Therefore, either an iterative process of narrowing the parameter range to reach a linear relation or a different DoE with more than two parameter levels should be used, as done by (Rackl & Hanley 2017). The better quality of prediction is of course paid by a higher number of simulations. To overcome this a combination of parameter screening with a simple DoE to reduce the number of parameters and a detailed DoE with few parameters would be an option.

5 Nomenclature

Abbreviations

CDT	Constant Directional Torque
CFD	Computational Fluid Dynamics
DEM	Discrete Element Method
DoE	Design of Experiments
DPI	Dry Powder Inhaler
FEM	Finite Element Method
LH100	Lactohale® 100
LH220	Lactohale® 220
MPFEM	Multi Particle Finite Element Method
VdW	Van der Waals
SF	Scale Factor

Symbols

A_H	Hamaker Constant
bi	single parameter regression coefficient
b_k	interaction regression coefficient
D	Surface Distance
D_{min}	minimum VdW Distance
D_{max}	VdW cut off Distance
d	Diameter
e	Coefficient of restitution
E_i	Effect of single parameter
E_k	Effect of two parameter interaction
F	Force
F_{hys}	Hysteresis Force of the Luding Model
F_0	Luding Pull off Force
$F_{n,\,Luding}$	Total normal Force given by Luding Contact Model
$F_{n,CC}$	Normal Force used in Coulomb criterion
F_{VdW}	Normal Force due to VdW Cohesion
f	Factor
G	Shear Modulus
h	Height
k_1	Particle Load Stiffness
k_2	Particle Unload Stiffness
k_2^*	Interpolated Particle Unloading/Reloading stiffness

k_c	Particle Cohesion Stiffness
k_{load}	Bulk Load Stiffness
k_{unload}	Bulk Unload Stiffness
k_{YL}	Slope of the Yield Locus
m	Mass
r	Radius
T	Torque
t	Time
$t_{Rayleigh}$	Rayleigh time stet
v	Speed
w	Rotational Speed
$w_{r,shear}$	circumferential relative speed of the particles in contact
x	Position
Y	Youngs Modulus
y	Response

Greek Symbols

β	compressibility
γ	damping coefficient
δ	overlap
δ'	Dimensionless Overlap
δ_{max}	Maximum Overlap Within Luding Load Cycle
δ^*_{max}	Maximum possible Overlap used in Luding Model
δ_0	Overlap at $F_{hys}=F_0$
ε	Deviation
φ_x	Wall Friction Angle
ϕ_f	Plasticity Depth
μ	coefficient of friction
ν	Poisson Ratio
ρ	density
σ	Normal Stress
σ_{pre}	Normal Stress in Pre-Shear Test
σ_x	Normal Stress at Yield Point
τ	Shear Stress
τ_1	Yield Shear Stress
τ_0	Intercept of the Yield Locus

ξ	Parameter value

Subscripts

0	at zero force level
1	Direction 1, loading
2	Direction 2, unloading
c	cohesion
d	dynamic
eff	effective
h	high
hys	hysteresis
i	Particle i
j	Particle j
pre	pre-shear
l	low
n	normal
real	unscaled value
r,roll	rolling
s	static
wall	particle-wall interaction
t	tangential
tens	tension

6 List of Figures

7 List of Tables

8 Literature

Ai, J. et al., 2011. Assessment of rolling resistance models in discrete element simulations. *Powder Technology*, 206(3), pp.269–282. Available at: http://dx.doi.org/10.1016/j.powtec.2010.09.030.

Bramböck, A., 2017. Correlation of Bulk Properties and DEM Contact Models for Cohesive Powders.

Coetzee, C.J., 2016. Calibration of the discrete element method and the effect of particle shape. *Powder Technology*, 297, pp.50–70. Available at: http://dx.doi.org/10.1016/j.powtec.2016.04.003.

Coetzee, C.J., 2017. Review: Calibration of the discrete element method. *Powder Technology*, 310, pp.104–142. Available at: http://dx.doi.org/10.1016/j.powtec.2017.01.015.

Coetzee, C.J. & Els, D.N.J., 2009. Calibration of discrete element parameters and the modelling of silo discharge and bucket filling. *Computers and Electronics in Agriculture*, 65(2), pp.198–212.

Cundall, P.A. & Strack, O.D.L., 1979. Cundall_Strack_1979. *Geeotechnique*, (29), pp.47–65.

Das, S.C. et al., 2013. Importance of particle size and shape on the tensile strength distribution and de-agglomeration of cohesive powders. *Powder Technology*, 249, pp.297–303. Available at: http://dx.doi.org/10.1016/j.powtec.2013.08.034.

DFE Pharma, Product information on Lactohale 220. Available at: https://www.dfepharma.com/en/excipients/inhalation-lactose/lactohale-220.aspx.

DFE Pharma, Productinformation on Lactohale 100. Available at: https://www.dfepharma.com/en/excipients/inhalation-lactose/lactohale-100.aspx.

Diarra, H. et al., 2013. FEM simulation of the die compaction of pharmaceutical products: Influence of visco-elastic phenomena and comparison with experiments. *International Journal of Pharmaceutics*, 453(2), pp.389–394. Available at: http://dx.doi.org/10.1016/j.ijpharm.2013.05.038.

Fisher, R.A., 1935. The design of experiments.

Gantt, J.A. & Gatzke, E.P., 2005. High-shear granulation modeling using a discrete element

simulation approach. *Powder Technology*, 156(2–3), pp.195–212.

Gethin, D.T. et al., 2001. Numerical comparison of a deformable discrete element model and an equivalentcontinuum analysis for the compaction of ductile porous material. *Computers and Structures*, 79, pp.1287–1294.

Girardi, M., Radl, S. & Sundaresan, S., 2016. Simulating wet gas-solid fluidized beds using coarse-grid CFD-DEM. *Chemical Engineering Science*, 144, pp.224–238. Available at: http://dx.doi.org/10.1016/j.ces.2016.01.017.

Han, P. et al., 2017. Particulate scale MPFEM modeling on compaction of Fe and Al composite powders. *Powder Technology*, 314, pp.69–77. Available at: http://dx.doi.org/10.1016/j.powtec.2016.11.021.

Hertz, 1882. Ueber die Berührung fester elastischer Körper. *Journal für die reine und angewandte Mathematik (Crelle's Journal)*, 1882, p.156. Available at: https://www.degruyter.com/view/j/crll.1882.issue-92/crll.1882.92.156/crll.1882.92.156.xml.

Horabik, J. & Molenda, M., 2016. Parameters and contact models for DEM simulations of agricultural granular materials: A review. *Biosystems Engineering*, 147, pp.206–225.

Ji, S., Hanes, D.M. & Shen, H.H., 2009. Comparisons of physical experiment and discrete element simulations of sheared granular materials in an annular shear cell. *Mechanics of Materials*, 41(6), pp.764–776. Available at: http://dx.doi.org/10.1016/j.mechmat.2009.01.029.

Khoei, A.R. & Lewis, R.W., 1999. Adaptive finite element remeshing in a large deformation analysis of metal powder forming. *Int. J. Numer. Meth. Engng*, 45(June 1998), pp.801–820.

Kinnunen, H. et al., 2015. Extrinsic lactose fines improve dry powder inhaler formulation performance of a cohesive batch of budesonide via agglomerate formation and consequential co-deposition. *International Journal of Pharmaceutics*, 478(1), pp.53–59. Available at: http://dx.doi.org/10.1016/j.ijpharm.2014.11.019.

Kleppmann, W., 2013. Versuchsplanung. In *Versuchsplanung*. Carl Hanser Verlag GmbH & Co. KG, pp. 129–164. Available at: https://doi.org/10.3139/9783446437913.fm.

Kloss, C. et al., 2012. Models, algorithms and validation for opensource DEM and CFD–DEM. *Progress in Computational Fluid Dynamics, an International Journal*, 12(2–3), pp.140–152.

Available at: https://www.inderscienceonline.com/doi/abs/10.1504/PCFD.2012.047457.

Li, G. et al., 2001. Recent development and applications of three-dimensional finite element modeling in bulk forming processes. *Journal of Materials Processing Technology*, 113(1–3), pp.40–45. Available at: http://www.sciencedirect.com/science/article/pii/S0924013601005908.

Loidolt, P., Madlmeir, S. & Khinast, J.G., 2017. Mechanistic modeling of a capsule filling process. *International Journal of Pharmaceutics*, 532(1), pp.47–54. Available at: http://dx.doi.org/10.1016/j.ijpharm.2017.08.125.

Loidolt, P., Ulz, M.H. & Khinast, J., 2018. Modeling yield properties of compacted powder using a multi-particle finite element model with cohesive contacts. *Powder Technology*, 336, pp.426–440. Available at: https://linkinghub.elsevier.com/retrieve/pii/S003259101830456X.

Luding, S., 2008. Cohesive, frictional powders: Contact models for tension. *Granular Matter*, 10(4), pp.235–246.

Madlmeir, S., 2018. DEM simulation of the dosator capsule filling process.

Mishra, B.K., 2003. A review of computer simulation of tumbling mills by the discrete element method: Part I-contact mechanics. *International Journal of Mineral Processing*, 71(1–4), pp.73–93.

NIST/SEMATECH, 2012. *e-Handbook of Statistical Methods*, Available at: https://www.itl.nist.gov/div898/handbook/pri/section3/eqns/2to8m3.txt.

Oñate, E. et al., 2008. Advances in the particle finite element method for the analysis of fluid-multibody interaction and bed erosion in free surface flows. *Computer Methods in Applied Mechanics and Engineering*, 197(19–20), pp.1777–1800.

Parteli, E.J.R. et al., 2014. Attractive particle interaction forces and packing density of fine glass powders. *Scientific Reports*, 4, p.6227. Available at: http://www.nature.com/doifinder/10.1038/srep06227.

Procopio, A.T. & Zavaliangos, A., 2005. Simulation of multi-axial compaction of granular media from loose to high relative densities. *Journal of the Mechanics and Physics of Solids*, 53(7), pp.1523–1551.

Rackl, M. & Hanley, K.J., 2017. A methodical calibration procedure for discrete element models. *Powder Technology*, 307, pp.73–83. Available at: http://dx.doi.org/10.1016/j.powtec.2016.11.048.

Radeke, C.A., Glasser, B.J. & Khinast, J.G., 2010. Large-scale powder mixer simulations using massively parallel GPUarchitectures. *Chemical Engineering Science*, 65(24), pp.6435–6442.

Di Renzo, A. & Di Maio, F.P., 2004. Comparison of contact-force models for the simulation of collisions in DEM-based granular flow codes. *Chemical Engineering Science*, 59(3), pp.525–541. Available at: http://linkinghub.elsevier.com/retrieve/pii/S0009250903005414 [Accessed November 20, 2014].

Schulze, D., 2009. *Pulver und Schüttgüter*, Springer Berlin Heidelberg.

Schweiger, A. & Zimmermann, I., 1998. A new approach for the measurement of the tensile strength of powders. *Powder Technology*, 101(June 1998), pp.1–9.

Shalash, A.O. et al., 2017. The Relationship Between the Permeability and the Performance of Carrier-Based Dry Powder Inhalation Mixtures: New Insights and Practical Guidance. *AAPS PharmSciTech*, 19(2), pp.912–922. Available at: http://link.springer.com/10.1208/s12249-017-0898-7.

Soltanbeigi, B. et al., 2018. DEM study of mechanical characteristics of multi-spherical and superquadric particles at micro and macro scales. *Powder Technology*, 329, pp.288–303. Available at: https://doi.org/10.1016/j.powtec.2018.01.082.

Zhu, H.P. et al., 2008. Discrete particle simulation of particulate systems: A review of major applications and findings. *Chemical Engineering Science*, 63(23), pp.5728–5770.

9 Appendix

Table 17: Parameter combinations used for the screening for important parameters

	$A_{H,real}$ 10^{-19} [J]	r_{real} [μm]	μ_s [-]	μ_d/μ_s [-]	Y_{real} [MPa]	k_2/k_1 [-]	k_c/k_1 [-]	k_t/k_1 [-]	e [-]	γ_t/γ_n [-]	ϕ_f [-]	μ_r [-]
0	150	50	0.3	1	50	20	5	1	0.8	1	0.2	0.2
1	150	50	0.3	1	10	2	5	1	0.5	0.2	0.2	0.2
2	150	50	0.3	0.5	50	2	5	0.2	0.8	1	0.02	0.02
3	150	50	0.3	0.5	10	20	5	0.2	0.5	0.2	0.02	0.02
4	150	50	0.1	1	50	2	0.5	1	0.8	0.2	0.02	0.02
5	150	50	0.1	1	10	20	0.5	1	0.5	1	0.02	0.02
6	150	50	0.1	0.5	50	20	0.5	0.2	0.8	0.2	0.2	0.2
7	150	50	0.1	0.5	10	2	0.5	0.2	0.5	1	0.2	0.2
8	150	5	0.3	1	50	2	0.5	0.2	0.5	1	0.2	0.02
9	150	5	0.3	1	10	20	0.5	0.2	0.8	0.2	0.2	0.02
10	150	5	0.3	0.5	50	20	0.5	1	0.5	1	0.02	0.2
11	150	5	0.3	0.5	10	2	0.5	1	0.8	0.2	0.02	0.2
12	150	5	0.1	1	50	20	5	0.2	0.5	0.2	0.02	0.2
13	150	5	0.1	1	10	2	5	0.2	0.8	1	0.02	0.2
14	150	5	0.1	0.5	50	2	5	1	0.5	0.2	0.2	0.02
15	150	5	0.1	0.5	10	20	5	1	0.8	1	0.2	0.02
16	10	50	0.3	1	50	2	0.5	0.2	0.5	0.2	0.02	0.2
17	10	50	0.3	1	10	20	0.5	0.2	0.8	1	0.02	0.2
18	10	50	0.3	0.5	50	20	0.5	1	0.5	0.2	0.2	0.02
19	10	50	0.3	0.5	10	2	0.5	1	0.8	1	0.2	0.02
20	10	50	0.1	1	50	20	5	0.2	0.5	1	0.2	0.02
21	10	50	0.1	1	10	2	5	0.2	0.8	0.2	0.2	0.02
22	10	50	0.1	0.5	50	2	5	1	0.5	1	0.02	0.2
23	10	50	0.1	0.5	10	20	5	1	0.8	0.2	0.02	0.2
24	10	5	0.3	1	50	20	5	1	0.8	0.2	0.02	0.02
25	10	5	0.3	1	10	2	5	1	0.5	1	0.02	0.02
26	10	5	0.3	0.5	50	2	5	0.2	0.8	0.2	0.2	0.2
27	10	5	0.3	0.5	10	20	5	0.2	0.5	1	0.2	0.2
28	10	5	0.1	1	50	2	0.5	1	0.8	1	0.2	0.2
29	10	5	0.1	1	10	20	0.5	1	0.5	0.2	0.2	0.2
30	10	5	0.1	0.5	50	20	0.5	0.2	0.8	1	0.02	0.02
31	10	5	0.1	0.5	10	2	0.5	0.2	0.5	0.2	0.02	0.02
32	80	27.5	0.2	0.75	30	11	2.75	0.6	0.65	0.6	0.11	0.11

Table 18: Parameter combinations used for the large parameter range for calibration

	$A_{H,real}$ 10^{-19} [J]	k_2/k_1 [-]	μ_s [-]	Y_{real} [MPa]	ϕ_f [-]	r_{real} [µm]	μ_r [-]	k_c/k_1 [-]
0	100	20	1.2	50	0.2	50	0.3	0.3
1	100	20	1.2	50	0.02	50	0.3	0.03
2	100	20	1.2	10	0.2	50	0.03	0.03
3	100	20	1.2	10	0.02	50	0.03	0.3
4	100	20	0.5	50	0.2	5	0.3	0.03
5	100	20	0.5	50	0.02	5	0.3	0.3
6	100	20	0.5	10	0.2	5	0.03	0.3
7	100	20	0.5	10	0.02	5	0.03	0.03
8	100	2	1.2	50	0.2	5	0.02	0.03
9	100	2	1.2	50	0.02	5	0.2	0.03
10	100	2	1.2	10	0.2	5	0.2	0.3
11	100	2	1.2	10	0.02	5	0.02	0.3
12	100	2	0.5	50	0.2	50	0.03	0.3
13	100	2	0.5	50	0.02	50	0.03	0.03
14	100	2	0.5	10	0.2	50	0.3	0.03
15	100	2	0.5	10	0.02	50	0.3	0.3
16	10	20	1.2	50	0.2	5	0.03	0.3
17	10	20	1.2	50	0.02	5	0.03	0.03
18	10	20	1.2	10	0.2	5	0.3	0.03
19	10	20	1.2	10	0.02	5	0.3	0.3
20	10	20	0.5	50	0.2	50	0.03	0.03
21	10	20	0.5	50	0.02	50	0.03	0.3
22	10	20	0.5	10	0.2	50	0.3	0.3
23	10	20	0.5	10	0.02	50	0.3	0.03
24	10	2	1.2	50	0.2	50	0.3	0.03
25	10	2	1.2	50	0.02	50	0.3	0.3
26	10	2	1.2	10	0.2	50	0.03	0.3
27	10	2	1.2	10	0.02	50	0.03	0.03
28	10	2	0.5	50	0.2	5	0.3	0.3
29	10	2	0.5	50	0.02	5	0.3	0.03
30	10	2	0.5	10	0.2	5	0.03	0.03
31	10	2	0.5	10	0.02	5	0.03	0.3
32	55	11	0.85	30	0.11	27.5	0.165	0.165

Main effect plots yielded for the parameter range used in 3.3.1

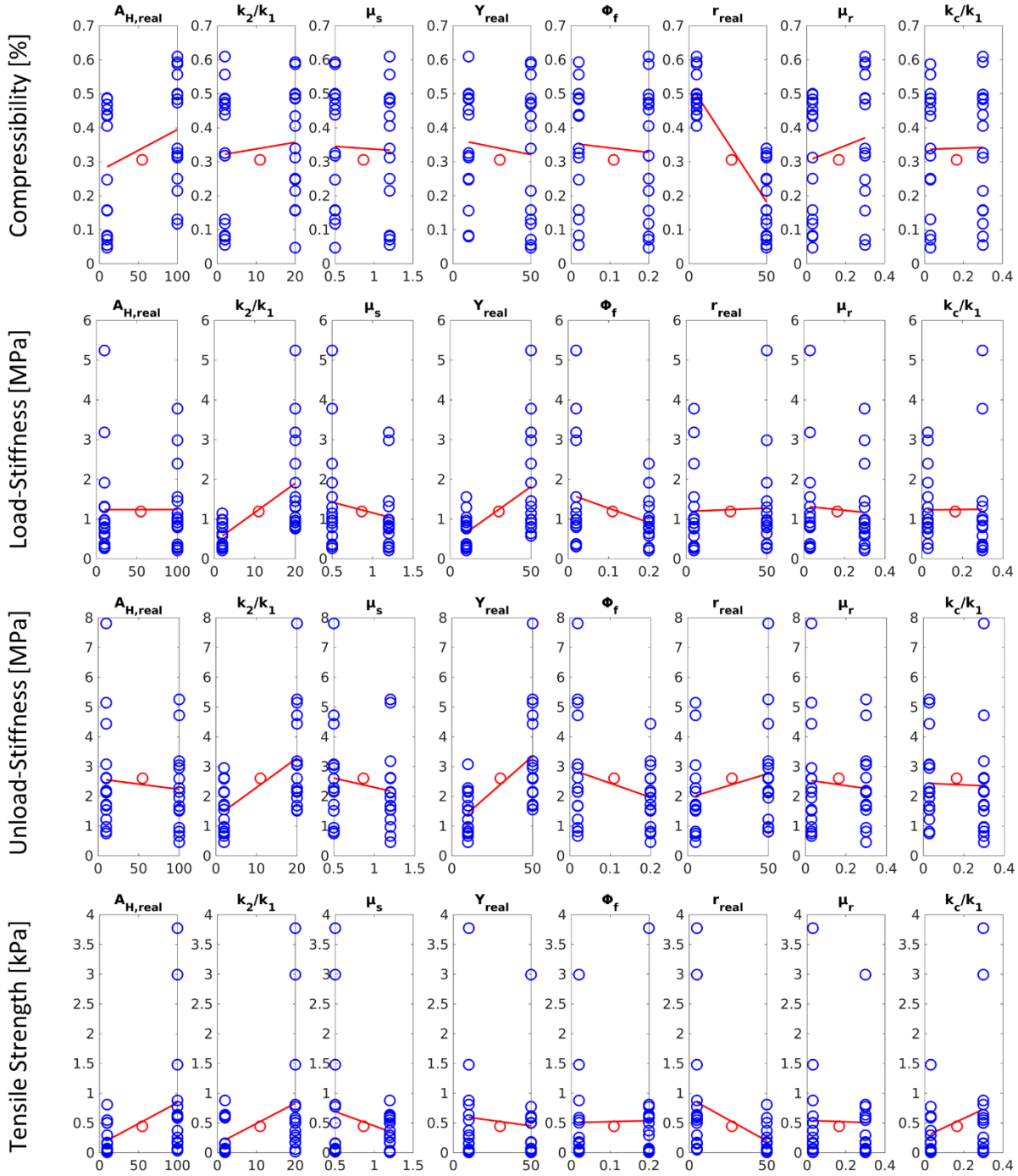

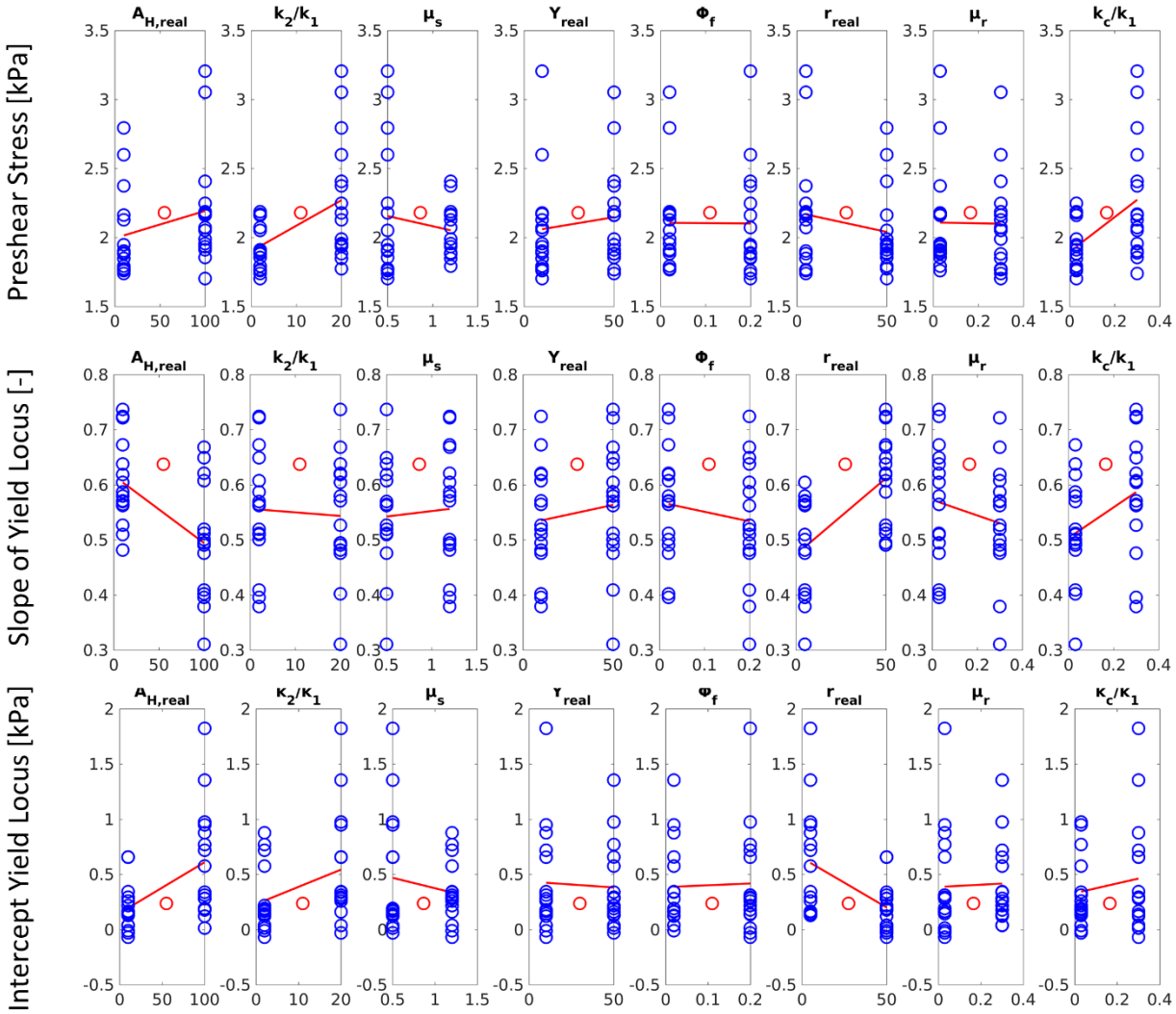

Table 19:Mean prediction errors in % for the DoE regression with and without taking two factor interactions into account for the parameter range used for the calibration of Lactohale® 100

	β	k_{load}	k_{unload}	σ_{tens}	τ_{pre}	τ_0	k_{YL}
without interaction	8.81	8.72	4.07	15.1	2.75	14.1	3.97
with interaction	2.63	0.82	0.532	4.65	0.902	4.16	1.68

Table 20:Mean prediction errors in % for the DoE regression with and without taking two factor interactions into account for the parameter range used for the calibration of Lactohale® 220

	β	k_{load}	k_{unload}	σ_{tens}	τ_{pre}	τ_0	k_{YL}
without interaction	1.48	9.5	4.71	18.9	2.25	19.5	5.25
with interaction	0.463	0.521	0.479	4.76	0.654	4.56	2.5

Table 21: Parameter set used for the simulation of hopper discharge

$A_{H,real}$	k_2/k_1	μ_{stat}	Y_{real}	ϕ_f	r_{real}	μ_r	k_c/k_1	$\mu_{s,wall}$
10^{-19} [J]	[-]	[-]	[MPa]	[-]	[µm]	[-]	[-]	[-]
50	12	0.6	21	0.0267	10	0.1	0.2667	0.2

Table 22: Results yielded for the powder used for hopper discharge

β	k_{load}	k_{unload}	σ_{tens}	τ_{pre}	τ_0	k_{YL}	φ_x
[%]	[MPa]	[MPa]	[kPa]	[kPa]	[kPa]	[-]	[°]
5.56	0.904	2.09	0.0739	1.75	0.14	0.487	